

# Synergism of type 1 metabotropic and ionotropic glutamate receptors in cerebellar molecular layer interneurons in vivo

Jin Bao<sup>1,2</sup>, Michael Graupner<sup>1</sup>, Guadalupe Astorga<sup>1†</sup>, Thibault Collin<sup>1</sup>, Abdelali Jalil<sup>1</sup>, Dwi Wahyu Indriati<sup>3‡</sup>, Jonathan Bradley<sup>1,4</sup>, Ryuichi Shigemoto<sup>3,5</sup>, Isabel Llano<sup>1\*</sup>

<sup>1</sup>Université de Paris, CNRS, SPPIN - Saints-Pères Paris Institute for the Neurosciences, Paris, France; <sup>2</sup>The Brain Cognition and Brain Disease Institute (BCBDI), Shenzhen Institutes of Advanced Technology, Chinese Academy of Sciences; Shenzhen-Hong Kong Institute of Brain Science-Shenzhen Fundamental Research Institutions, Shenzhen, China; <sup>3</sup>Division of Cerebral Structure, National Institute for Physiological Sciences, The Graduate University for Advanced Studies (Sokendai), Okazaki, Japan; <sup>4</sup>Institut de Biologie de l'École Normale Supérieure (IBENS), École Normale Supérieure, CNRS, INSERM, PSL Research University, Paris, France; <sup>5</sup>IST Austria, Klosterneuburg, Austria

\*For correspondence: isabel.llano@parisdescartes.fr

Present address: <sup>†</sup>The Rockefeller University, New York, United States; <sup>‡</sup>Department of Health, Faculty of Vocational Studies, Universitas Airlangga, Surabaya, Indonesia

Competing interests: The authors declare that no competing interests exist.

Funding: See page 18

Received: 11 March 2020

Accepted: 27 April 2020

Published: 13 May 2020

Reviewing editor: Yukiko Goda, RIKEN, Japan

© Copyright Bao et al. This article is distributed under the terms of the [Creative Commons Attribution License](https://creativecommons.org/licenses/by/4.0/), which permits unrestricted use and redistribution provided that the original author and source are credited.

**Abstract** Type 1 metabotropic glutamate receptors (mGluR1s) are key elements in neuronal signaling. While their function is well documented in slices, requirements for their activation in vivo are poorly understood. We examine this question in adult mice in vivo using 2-photon imaging of cerebellar molecular layer interneurons (MLIs) expressing GCaMP. In anesthetized mice, parallel fiber activation evokes beam-like Ca<sub>i</sub> rises in postsynaptic MLIs which depend on co-activation of mGluR1s and ionotropic glutamate receptors (iGluRs). In awake mice, blocking mGluR1 decreases Ca<sub>i</sub> rises associated with locomotion. In vitro studies and freeze-fracture electron microscopy show that the iGluR-mGluR1 interaction is synergistic and favored by close association of the two classes of receptors. Altogether our results suggest that mGluR1s, acting in synergy with iGluRs, potentially contribute to processing cerebellar neuronal signaling under physiological conditions.

## Introduction

A considerable body of data, spanning from genomics and structural studies of receptors to functional studies at the synaptic level, indicates that glutamate released at excitatory synapses of the mammalian nervous system binds to both ionotropic (iGluRs) and type 1 metabotropic receptors (mGluR1s) and engages a complex pattern of signaling pathways often involving a synergistic action of both receptors (reviewed in *Reiner and Levitz, 2018*). In the cerebellar cortex, glutamate released by parallel fibers (PFs) binds to receptors on Purkinje cells (PCs) and on molecular layer interneurons (MLIs), which form an interconnected circuit governing the output of the cerebellar cortex. Patterns of PF activity convey information on the sensorimotor state of the animal (review by *Jörntell, 2017*) and determine the recruitment of MLIs through PF-MLI synapses (*Bao et al., 2010*). From work in brain slices it is known that several types of iGluRs (*Carter and Regehr, 2000*) as well as mGluR1s (*Karakossian and Otis, 2004; Collin et al., 2009*) are activated in MLIs by synaptically released glutamate. Furthermore, it is well documented that the PF-MLI synapse is susceptible to activity-dependent modulation such that postsynaptic AMPARs can change their Ca<sup>2+</sup> permeability

in response to neuronal activity (Liu and Cull-Candy, 2000). This plastic shift in  $\text{Ca}^{2+}$  permeability has been linked to specific behavioral states (Liu et al., 2010) and it is thought to involve activation of mGluR1 (Kelly et al., 2009). As MLIs are key elements of the cerebellar circuit during motor behavior and cerebellar-dependent motor learning (Wulff et al., 2009; Jelitai et al., 2016; Gaffield and Christie, 2017; Rowan et al., 2018), examining mGluR1-mediated plasticity at PF-MLI synapses is of great importance in understanding cerebellar function.

In contrast to the wealth of knowledge from slice work, the contributions of iGluRs and mGluR1s to signaling in vivo have not been investigated in any detail. Yet significant differences between work in slices and in vivo may arise from morphological perturbations due to tissue slicing (Bak et al., 1980; Dzhala et al., 2012) and from changes in either glutamate homeostasis or in molecules involved in ionotropic and/or metabotropic glutamate signaling. To fill this knowledge gap, we analyze in the present work the role of mGluR1s in generating PF-evoked  $\text{Ca}_i$  signals in MLIs.

When investigating  $\text{Ca}_i$  rises induced by beam-activation of PFs in anesthetized mice, we ask:

1. Which conditions of PF stimulation lead to robust mGluR1 signaling?
2. Is there a synergy between iGluRs and mGluR1s at the PF-MLI synapse?

Using freeze-fracture electron microscopy, we ask:

1. What is the spatial distribution of AMPARs and mGluR1s at the PF-MLI synapse and what is its functional relevance in terms of mGluR1-iGluR interaction?

In awake mice, we ask:

1. Are mGluR1s activated during an ordinary motor task such as walking?

When considered together, our results strongly suggest that mGluR1s potentially contribute to cerebellar signaling under physiological conditions and furthermore, shed light on the nature of interactions between mGluR1- and iGluR-mediated signals.

## Results

### Activation of mGluR1s by repetitive PF stimulation

In order to assess MLI activity in vivo, we expressed the Genetically Encoded Calcium Indicators (GECIs) GCaMP3 or GCaMP5 by stereotaxic injections of floxed AAV viral vectors into the cerebellar cortex of adult parvalbumin (PV) Cre mice (*Pvalb-Cre*; see Materials and methods). Although both MLIs and Purkinje cells (PCs) are PV positive, the combined use of specific viral serotype (either AAV2/1 or AAV2/9) and of the human synapsin promoter to drive expression, resulted in the almost exclusive GECI expression in somata and neurites of MLIs (Figure 1A; see also Kuhn et al., 2012; Astorga et al., 2015). In a horizontal plane of focus, we observed a periodic narrow striped fluorescence pattern characteristic of the parasagittal organization of MLI neurites while the wider interspaced non-fluorescent stripes (about 10  $\mu\text{m}$  thick) correspond to unlabeled PC dendrites. The absence of GCaMP expression in PCs is further illustrated in Figure 1B (left panel), which shows no overlap between GCaMP3 and calbindin (CB), a protein that is absent from MLIs but has a strong expression in PCs. On the other hand, the proportion of PV(+), CB(-) MLIs was very high (Figure 1B, right panel) with over 90% of MLIs expressing GECI as early as 7 days after injection. The level of expression increased during the first 2 weeks post-injection, as shown in Figure 1—figure supplement 1. The rapid time course of expression, and the MLI specificity obtained, provide us with a highly favorable situation for MLI study (Astorga et al., 2015; Astorga et al., 2017).

To activate a narrow bundle of PFs, a theta glass pipette was introduced through the meninges until it reached the outermost molecular layer (Figure 1C). In order to avoid direct stimulation of the MLIs under study, the minimal distance between the area imaged and the pipette was 150  $\mu\text{m}$ . High frequency PF stimulation generated robust  $\text{Ca}_i$  rises in MLIs expressing GCaMP3 proteins and  $\Delta\text{F}/\text{F}_0$  images displayed a characteristic beam-shaped increase in MLI fluorescence along the PF orientation (Sullivan et al., 2005; Figure 1C). Increasing the train duration led to progressively larger peak  $\text{Ca}_i$  transients, with  $\Delta\text{F}/\text{F}_0$  values increasing from  $138.9 \pm 30.6\%$  for trains lasting 0.2 s to  $347 \pm 43\%$  for 1 s long trains (N = 18). An example for a representative MLI soma is displayed in Figure 1D and group data from 8 animals in Figure 1E.

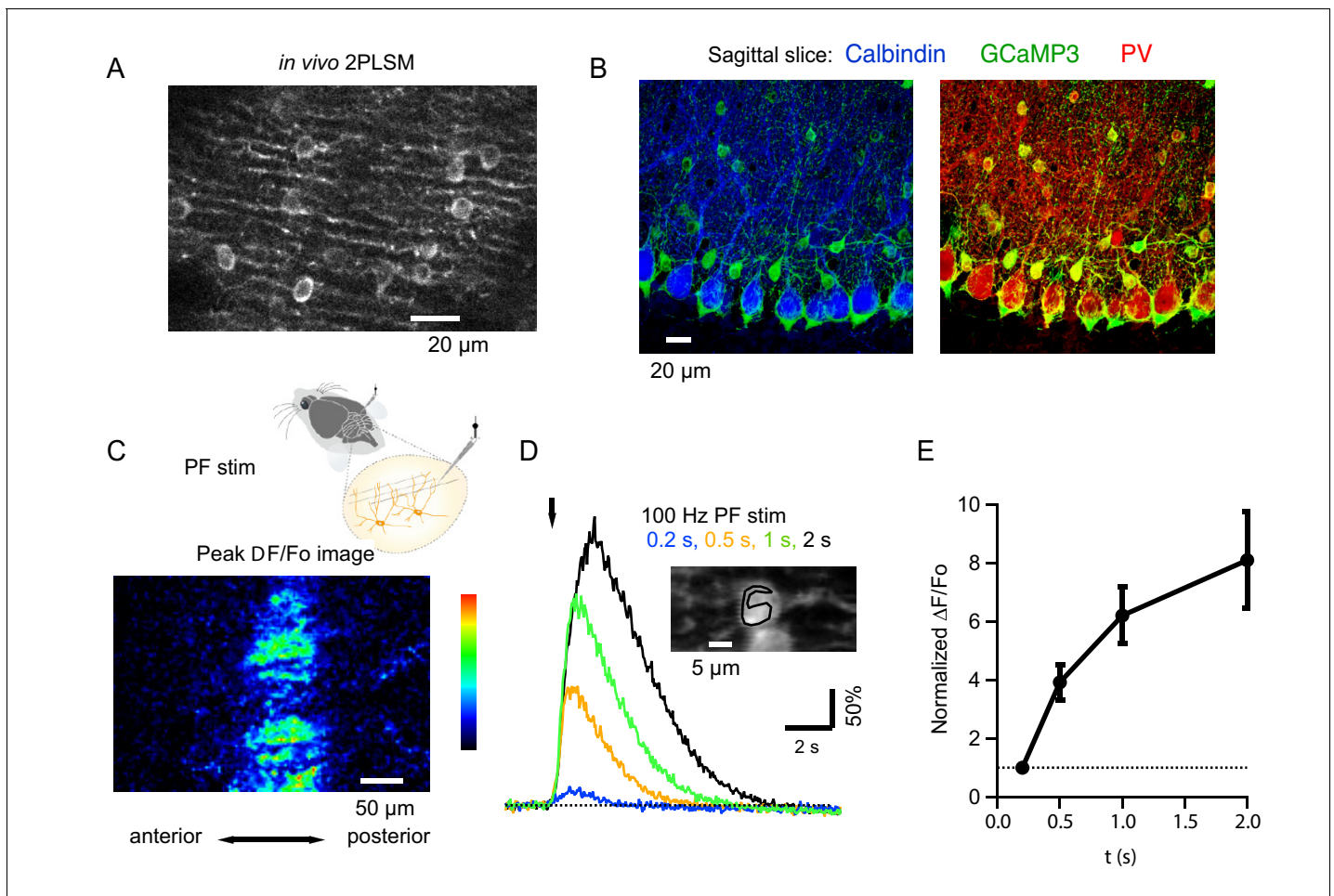


**Figure 1.** Beam activation in the cerebellar cortex of GCaMP3 expressing MLIs in vivo. (A) Two-photon laser scanning microscopy (2PLSM) image of the outermost cerebellar molecular layer in vivo shows cytoplasmic GCaMP3 and parasagittally aligned MLI neurites in a horizontal plane of focus. (B) Confocal stack projections of sagittal cerebellar slices from mice expressing AAV2/1hSyn.Flex.GCaMP3 on the background of PV-promoter driven CRE recombinase. *Left:* slice stained with an antibody against calbindin, a protein expressed in PCs and not in MLIs. Note that calbindin positive PCs do not express GCaMP3. *Right:* slice stained with an antibody against PV, a protein expressed in both PCs and MLIs. Note the colocalization between GCaMP3 and PV positive MLIs. (C) A beam pattern of  $\text{Ca}_i$  rise is illustrated by the  $\Delta\text{F}/\text{Fo}$  image at the peak of the fluorescence increase evoked in the molecular layer by a 0.5 s long PF stimulation at 100 Hz (horizontal plane of focus) using a bi-polar theta glass pipette as depicted in the cartoon. The highest value for the pseudo-color scale is 100%. (D) Time course of the somatic MLI  $\text{Ca}_i$  signals evoked in a representative MLI by 100 Hz PF stimulations of various durations. The arrow indicates the time of stimulation onset. The inset shows an average of pre-stimulus images to illustrate the ROI analyzed. (E) Average peak  $\Delta\text{F}/\text{Fo}$  values from 18 somata, normalized to the peak value for 200 ms trains at 100 Hz.

The online version of this article includes the following figure supplement(s) for figure 1:

**Figure supplement 1.** Expression of various GCaMP proteins in the cerebellar cortex.

To evaluate whether PF stimulation recruits mGluR1s in adult MLIs in vivo, as reported in slices for PCs (Finch and Augustine, 1998; Takechi et al., 1998) and MLIs (Karakossian and Otis, 2004; Collin et al., 2009), we compared  $\text{Ca}_i$  signals elicited by trains of PF stimulation (200  $\mu\text{s}$ -long pulses at 100 Hz) before and after addition of a specific mGluR1 antagonist, CPCCOEt, to the pool bathing the craniotomy. We found that CPCCOEt significantly decreased peak amplitudes for the somatic signals in vivo (Figure 2A1, A2 and B3). The stability of the normalized  $\Delta\text{F}/\text{Fo}$  values versus time plot in the control period, followed by a drastic drop after drug application, indicates that the decrease in  $\text{Ca}_i$  rises is due to mGluR1 block rather than to a run-down effect (Figure 2C). The remaining  $\text{Ca}_i$  signal was abolished in all cases by adding a combination of non-competitive antagonists of AMPARs and NMDARs (GYKI53655 and DCK respectively; Figure 2B, yellow traces), indicating the activation of iGluRs in MLIs. The finding of a complete block of the response by iGluR

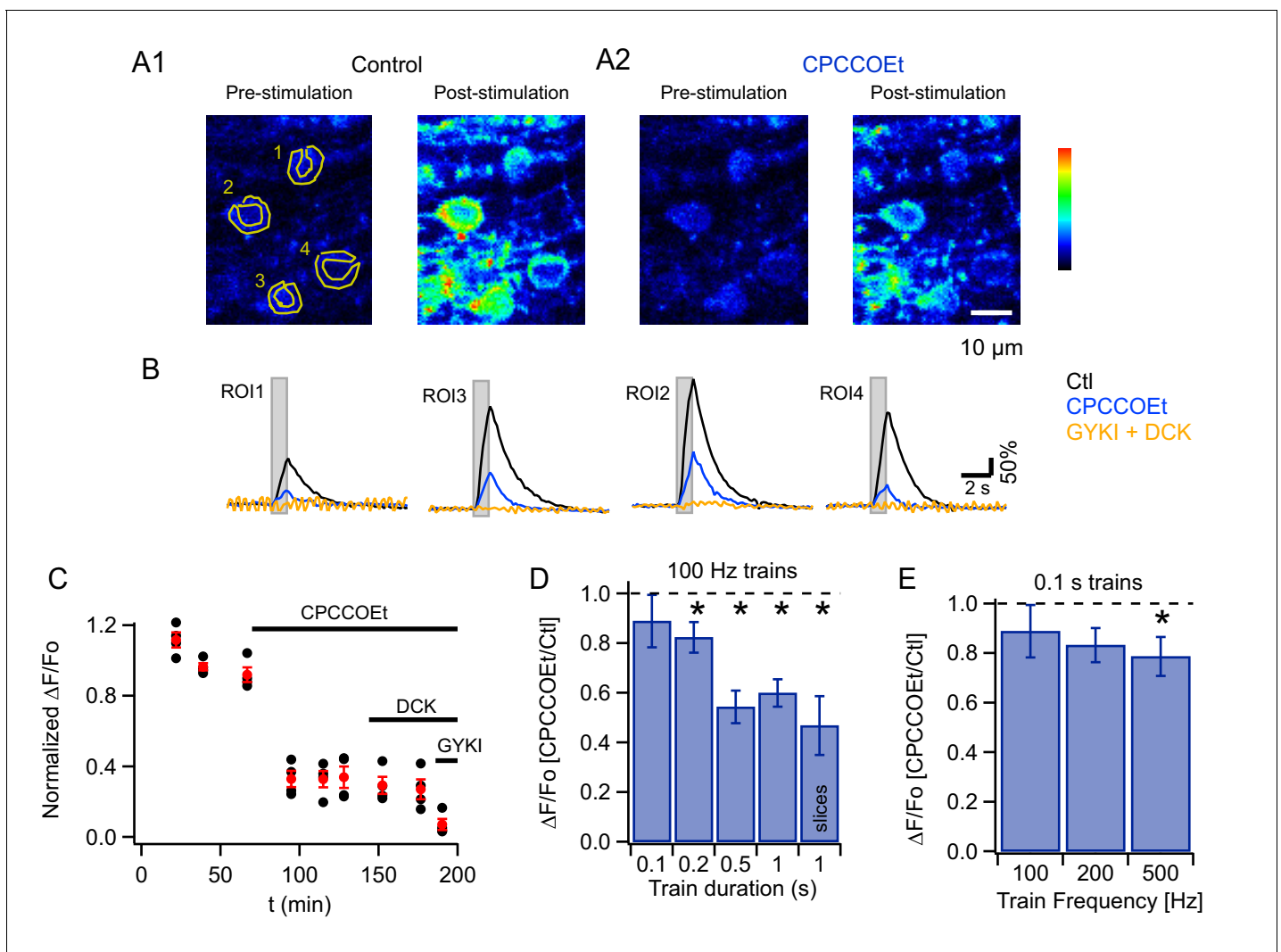


**Figure 2.** mGluR1s contribute to PF-evoked MLI somatic  $\text{Ca}_i$  rises. (A) Pharmacology of MLI  $\text{Ca}_i$  rises reported by GCaMP3 following PF stimulation. 2PLSM images at rest and at the peak of the response to PF stimulation (100 Hz for 1 s) in vivo in control (A1) and in CPCCOEt (A2). The pseudocolor scale in the images is expressed in Hz, calculated from the number of photons acquired during 10  $\mu\text{s}$  intervals. The highest counts are 2.1 MHz. Panel B shows  $\Delta\text{F}/\text{Fo}$  traces for the 4 ROIs drawn in the pre-stimulus image, in control (black), in 100  $\mu\text{M}$  CPCCOEt (blue) and after further addition of 300  $\mu\text{M}$  GYKI53655 and 100  $\mu\text{M}$  DCK (yellow). (C) Temporal evolution of the peak  $\text{Ca}_i$  rise for the experiment shown in B (black: individual cells; red: mean  $\pm$  sem). (D) Ratios of peak  $\Delta\text{F}/\text{Fo}$  amplitudes in CPCCOEt over control for 100 ms ( $n = 20$ ), 200 ms ( $n = 18$ ), 500 ms ( $n = 16$ ) and 1 s ( $n = 21$ ) trains of stimuli at 100 Hz in vivo and for 1 s stimulation at 100 Hz in vitro ( $n = 9$ ). Two-tailed  $p$  values from Wilcoxon tests are: 0.03,  $9.2 \times 10^{-5}$ ,  $4.8 \times 10^{-6}$  for 200 ms, 500 ms and 1 s trains in vivo and 0.008 for 1 s trains in vitro. Data from GCaMP3 and GCaMP5 expressing mice. (E) Ratios of  $\Delta\text{F}/\text{Fo}$  peak amplitudes in CPCCOEt over control for 100 ms trains applied at different frequencies ( $n = 20$ ; two-tailed  $p$  value from Wilcoxon test for 500 Hz: 0.04). Data from GCaMP5 expressing mice. The 100 Hz, 0.1 s bin is derived from the same data set as that used for the first bin in panel D.

antagonists ensures that the theta stimulation does not induce direct MLI activation. In two of the experiments DCK was added prior to GYKI53655; this failed to affect the CPCCOEt-insensitive  $\text{Ca}_i$  rises (example in **Figure 2C**), indicating that this residual signal depended on AMPARs but not on NMDARs. On average, ratios of peak  $\Delta\text{F}/\text{Fo}$  values in CPCCOEt over control in response to 1 s-long 100 Hz trains in vivo were similar to what we found in parallel experiments in slices (compare last two bars in **Figure 2D**; control peak  $\Delta\text{F}/\text{Fo}$  was  $347 \pm 43\%$  in vivo,  $n = 18$ ; and  $653 \pm 58\%$  in slices,  $n = 9$ ), arguing for a strong contribution of mGluR1s in both cases.

Analysis of in vivo  $\text{Ca}_i$  transients in the neuropil showed a significant reduction of peak  $\text{Ca}_i$  values by the mGluR1 antagonist, that was however smaller than the corresponding somatic reduction

(ratio of  $\Delta F/F_0$  in CPCCOEt to control values:  $0.73 \pm 0.03$  in neuropil vs  $0.47 \pm 0.10$  in somata; two-tailed p value from Wilcoxon test:  $2.1 \times 10^{-7}$ ). The smaller contribution of mGluR1s to the neuropil compared to the somatic signals may reflect the fact that when analyzing the neuropil we have no unambiguous way to discriminate dendrites versus axon. Therefore, our neuropil analysis reflects a mixed population of neurites, with dendrites having a presumably more robust mGluR1 signaling than axonal processes. Nonetheless, analysis of the neuropil allows us to confirm that mGluRs are engaged in dendrites, where the density of parallel fibers synapses is 3 fold higher than in the soma (Abrahamsson *et al.*, 2012).

Focusing again on somatic responses, we then examined the time window necessary for efficient mGluR1 recruitment *in vivo*, by quantifying the block by CPCCOEt for trains of different durations while keeping the stimulus frequency at 100 Hz. We found that as the train duration was shortened the extent of block decreased, such that with a 100 ms train essentially no mGluR1 component was observed (pooled data from 8 animals in **Figure 2D**).

We next asked whether increasing stimulation frequency enhances mGluR1 responses during short bursts of activity. This series of experiments was performed with GCaMP5, which yielded similar expression pattern as GCaMP3 (**Figure 1—figure supplement 1**) while offering a better dynamic range and improved signal-to-noise ratio (Akerboom *et al.*, 2012). Signals elicited by 100 ms-long trains at frequencies of 100, 200 and 500 Hz were compared before and after addition of mGluR1 blocker. Pooled data analysis (**Figure 2E**) indicated that a significant mGluR1 component was present only for the highest frequency tested (500 Hz). As before the signals were abolished by a combination of GYKI53655 and DCK.

## Activation of mGluRs in MLIs during locomotion

To examine the conditions for mGluR1 activation in behaving animals, we designed a forced locomotion paradigm combining a motorized, flat-surface treadmill with 2P resonant scanner imaging in the cerebellar cortex of head-fixed mice expressing GCaMP3 (**Figure 3A**) and assessed the effects of mGluR1 block on the resulting  $Ca_i$  signals. Drug access was enabled through holes in the coverslip ( $<500 \mu\text{m}$ ) and quantified by adding the fluorophore Alexa 594 to the drug containing solution (see Materials and methods and **Figure 3—figure supplement 1**). We aimed to reduce the inherent variability in awake behavioral paradigms by imposing a constant walking speed of 10 cm/s across recording sessions (see Materials and methods). 70–120 ROIs corresponding to MLI cell bodies were identified in each field of view ( $400 \times 400 \mu\text{m}$ , see **Figure 3B**). Many of the identified cells exhibited fluorescence dynamics correlated to locomotion, that is, the fluorescence signal was flat and low during resting periods while it increased and showed temporal dynamics during locomotion periods (**Figure 3C**). We performed this experiment on 4 animals and identified in total 313 soma present in the imaging planes in both conditions, that is, before and after drug application (see Materials and methods).

To directly measure the contribution of mGluR1s to the observed  $Ca_i$  transients, we repeated 6–14 forced locomotion recordings before and after application of CPCCOEt in four animals (compare **Figure 3C and D**). We then quantified the fluorescence during a 15 s period of maximal speed motorization (between 10 and 25 s in the recordings, **Figure 3C,D**, dark shaded areas; see Materials and methods). As we aimed at focusing on the large fluorescence increases, we extracted the 75th percentile of the  $\Delta F/F_{\text{rest}}$  trace per cell during the locomotion period, hereon referred to as *locomotion fluorescence* (**Figure 3E**). We observed an overall reduction in locomotion fluorescence with increasing number of recordings, which was shared across all ROIs (see **Figure 3E**). To remove this decay trend and single out drug-induced changes in locomotion fluorescence, a single exponential decay function was fitted to all *pre-drug* data-points per individual ROI and subtracted from *all* recordings of this ROI (compare **Figure 3E and F**, see Materials and methods). In control conditions,  $\Delta F/F_{\text{rest}}$  signals during locomotion had peak values of  $128.2 \pm 8.5\%$  (313 ROIs from 4 mice). We then compared the mean level of locomotion fluorescence before drug application to the change in locomotion fluorescence after drug application (**Figure 3G**). Individual cells showed significant increases (red symbols in **Figure 3G**), decreases (blue symbols; note large reduction in example cells coded by orange, burgundy and blue in **Figure 3E and F**) or no significant change (gray symbols) in their after-drug locomotion fluorescence compared to before-drug recordings. Nevertheless, the direction and the amplitude of fluorescence changes appeared to be predicted by the overall level of pre-drug locomotion fluorescence. Indeed, a linear regression analysis on all the cells gave a

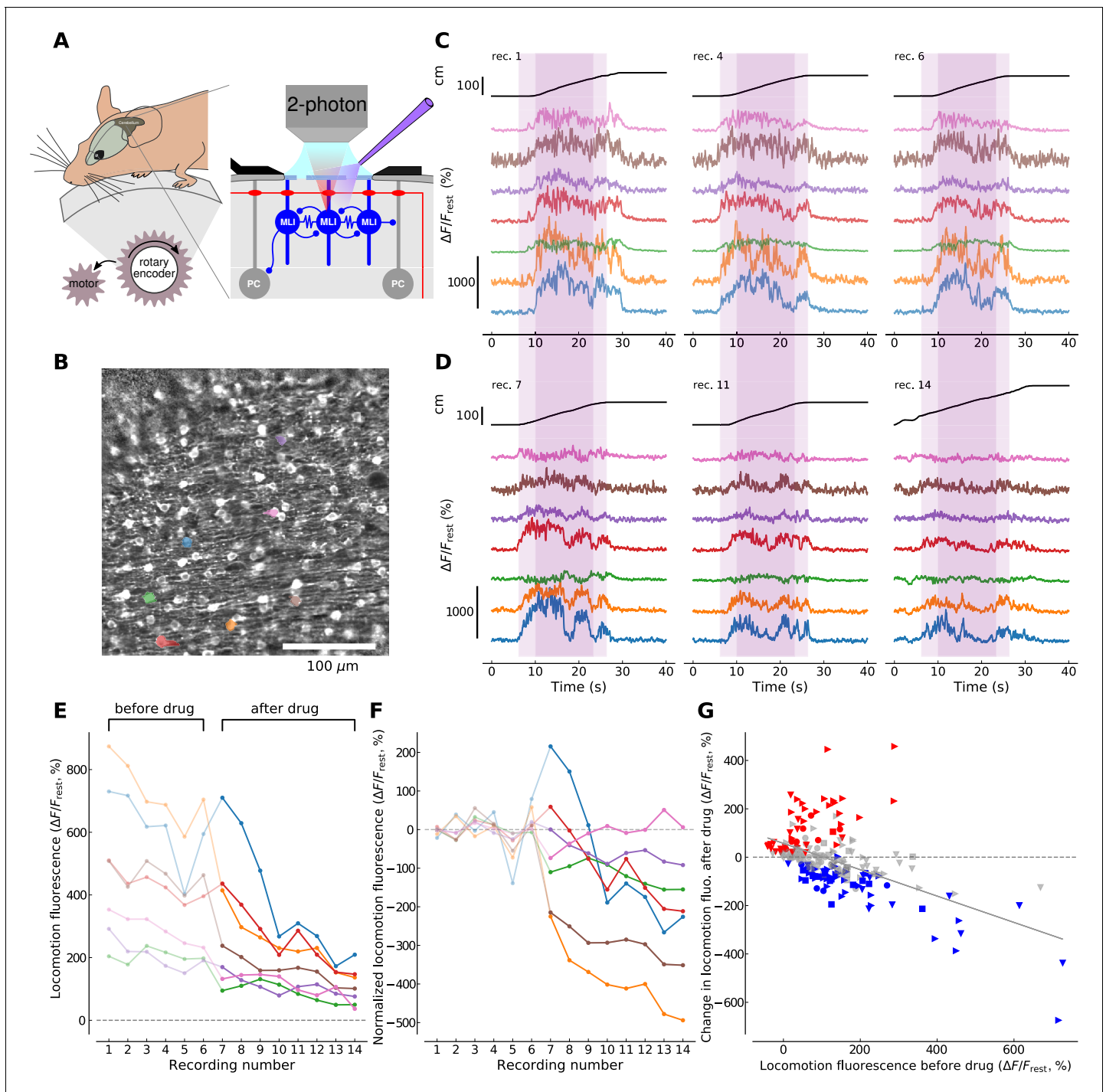


**Figure 3.** mGluR1s contribute to large-amplitude, locomotion-related  $\text{Ca}^{2+}$  activity in MLIs in the medial cerebellum. (A) Illustration of the forced locomotion experiment with simultaneous calcium imaging of MLIs. Mice can walk freely but the treadmill is motorized during a 20 s period, corresponding to the area shaded in purple in C and D between 6 and 26 s (dark purple corresponds to the 15 s maximal speed motorization period between 10 and 25 s of the recordings). At the right, a simplified circuit diagram of the cerebellar molecular and Purkinje cell layer illustrating craniotomy, 2 photon scanning and drug delivery. (B) Horizontal view of viral-mediated GCaMP3 expression in MLIs of a *Pvalb-Cre* mouse. Example ROIs are colored (see panels C,D,E,F). (C)  $\text{Ca}^{2+}$  responses during three non-consecutive locomotion recordings (recording number upper left; recordings repeated every 2–4 min, see Materials and methods). Top black traces show the distance traveled by the mouse during the recordings. Bottom traces show fluorescence for 7 randomly chosen example ROIs corresponding to individual cell bodies (see color-coded regions in B). The time period used for analysis is shaded in dark purple. (D) Same depiction as in (C) but after the application of CPCCOEt. (E) Calcium responses before and after CPCCOEt application. The 75<sup>th</sup> percentile of the fluorescence trace during the maximal-speed locomotion period [10, 25] s, dark purple shaded.

Figure 3 continued

region in (C,D) is shown as a function of the recording number. For this example mouse (animal #2), 6 recordings before- and 8 after drug delivery were performed. (F) Calcium activity normalized to pre-drug baseline. The pre-drug decay in fluorescence was subtracted from all points per ROI (see Materials and methods for details). Data for the same ROIs is shown in the same color in panels (B-F). Data points before CPCCOEt application are in pale color, data after drug delivery in dark color. (G) Change in fluorescence with CPCCOEt vs. pre-drug baseline data from all animals ( $N_{\text{animals}} = 4$ ) and ROIs ( $N_{\text{ROIs}} = 313$ ). The change in fluorescence is shown as a function of the pre-drug baseline fluorescence during locomotion. Data from each animal is plotted with the same symbols. The color of each symbol indicates whether a significant increase (red,  $p < 0.01$ , T-test), decrease (blue,  $p < 0.01$ , T-test) or no change (gray) has been observed when comparing baseline locomotion fluorescence with fluorescence after CPCCOEt application (see Materials and methods for more details). The linear regression on all points yields a correlation of  $-0.547$  with  $p$ -value  $< 0.0001$ , explaining 30.0% of the variance in the data.

The online version of this article includes the following figure supplement(s) for figure 3:

**Figure supplement 1.** Summary of Alexa 594 fluorescence changes related to drug application for all animals.

**Figure supplement 2.** Comparison of fluorescence fluctuations and level during the recordings at 820 nm excitation wavelength with respect to the runs at 910 nm.

correlation of  $-0.547$  ( $R^2 = 0.3$ ,  $p < 0.0001$ ) meaning that a more probable decrease in  $\text{Ca}_i$  signal happened after CPCCOEt application if a higher fluorescence response was elicited during locomotion before drug application. These results suggest that under control conditions large signals are more likely to involve mGluR1s than small signals, in accord with the finding that longer or higher frequency PF stimulations are more successful in recruiting mGluR1 (Figure 2D and E). Altogether, the experiments argue for an involvement of mGluR1 in physiologically relevant situations.

### Synergy between iGluRs and mGluR1s is not mediated by $\text{Ca}^{2+}$ -permeable AMPARs

We next investigated whether iGluR activation was required for the mGluR1-linked  $\text{Ca}_i$  increases at PF-MLI synapses, as reported previously for PF-PC synapses (Okubo et al., 2004). We found that simultaneous addition of GYKI53655 and DCK (which together should abolish iGluR activation) strongly decreased PF-evoked  $\text{Ca}_i$  rises for all train durations tested in slices as well as in vivo (Figure 4A and B). The extent of this inhibition was much larger than the value expected from the earlier results of Figure 2 if the fractions of inhibition by ionotropic and metabotropic blockers were independent. Thus, considering that CPCCOEt blocks close to 50% of the signal elicited by a 100 Hz stimulation train lasting 1 s (ratio of drug to control:  $0.47 \pm 0.12$ ; Figure 2D), the block by iGluRs would be expected to be around 50%. But the effect of iGluR block is much larger: for the same 100 Hz, 1 s long train the drugs block 94% of the response (ratio of drugs to control:  $0.06 \pm 0.01$ ; Figure 4B). This suggests that while responses to short trains of PF stimulation are governed mainly by iGluRs, synergy between iGluRs and mGluR1s occurs at the PF-MLI synapse during long trains. Earlier work in slices has shown that mGluR1-dependent  $\text{Ca}_i$  responses in MLIs depend on  $\text{Ca}^{2+}$  entry (Collin et al., 2009). Therefore, we hypothesized that the synergy between iGluRs and mGluR1s arises either from  $\text{Ca}^{2+}$ -influx through  $\text{Ca}^{2+}$ -permeable iGluRs, or from voltage-gated  $\text{Ca}^{2+}$ -entry following iGluR-induced depolarization.

Under certain conditions,  $\text{Ca}^{2+}$ -permeant AMPARs (CP-AMPA) occur at the PF-MLI synapse (Cull-Candy et al., 2006; Soler-Llavina and Sabatini, 2006). We therefore tested in vivo the effect of IEM1460, which inhibits preferentially CP-AMPA (Magazanik et al., 1997). We found that this compound had no effect on the PF-evoked  $\text{Ca}_i$  increases measured from the soma or the neuropil (Figure 4C and D; ratios of control to IEM:  $1.2 \pm 0.05$  and  $1.0 \pm 0.06$  for 200 ms and 1 s trains at 100 Hz;  $n = 6$  somas from 2 animals), suggesting a lack of  $\text{Ca}^{2+}$ -permeability for AMPARs in MLIs of adult mice. To test this possibility further, we next assessed the  $\text{Ca}^{2+}$  permeability of AMPARs in adult MLIs in slices by analyzing the I-V relations of currents evoked by uncaging of MNI glutamate (Figure 5A). All MLIs tested ( $n = 7$ ) yielded linear I-V relations characteristic of  $\text{Ca}^{2+}$  impermeable AMPARs (Cull-Candy et al., 2006; Figure 5B). Therefore, the synergistic dependence on iGluRs cannot be attributed to  $\text{Ca}^{2+}$  flux through AMPARs. Overall, in contrast to findings in the juvenile cerebellum (Cull-Candy et al., 2006; Soler-Llavina and Sabatini, 2006), we did not detect CP-AMPA in adult cerebellar MLIs either in slices or in vivo. These data indicate that AMPARs lose their  $\text{Ca}^{2+}$  permeability during development, a developmental switch already reported for glutamatergic synapses in different brain regions (Kumar et al., 2002; Eybalin et al., 2004; Isaac et al., 2007).

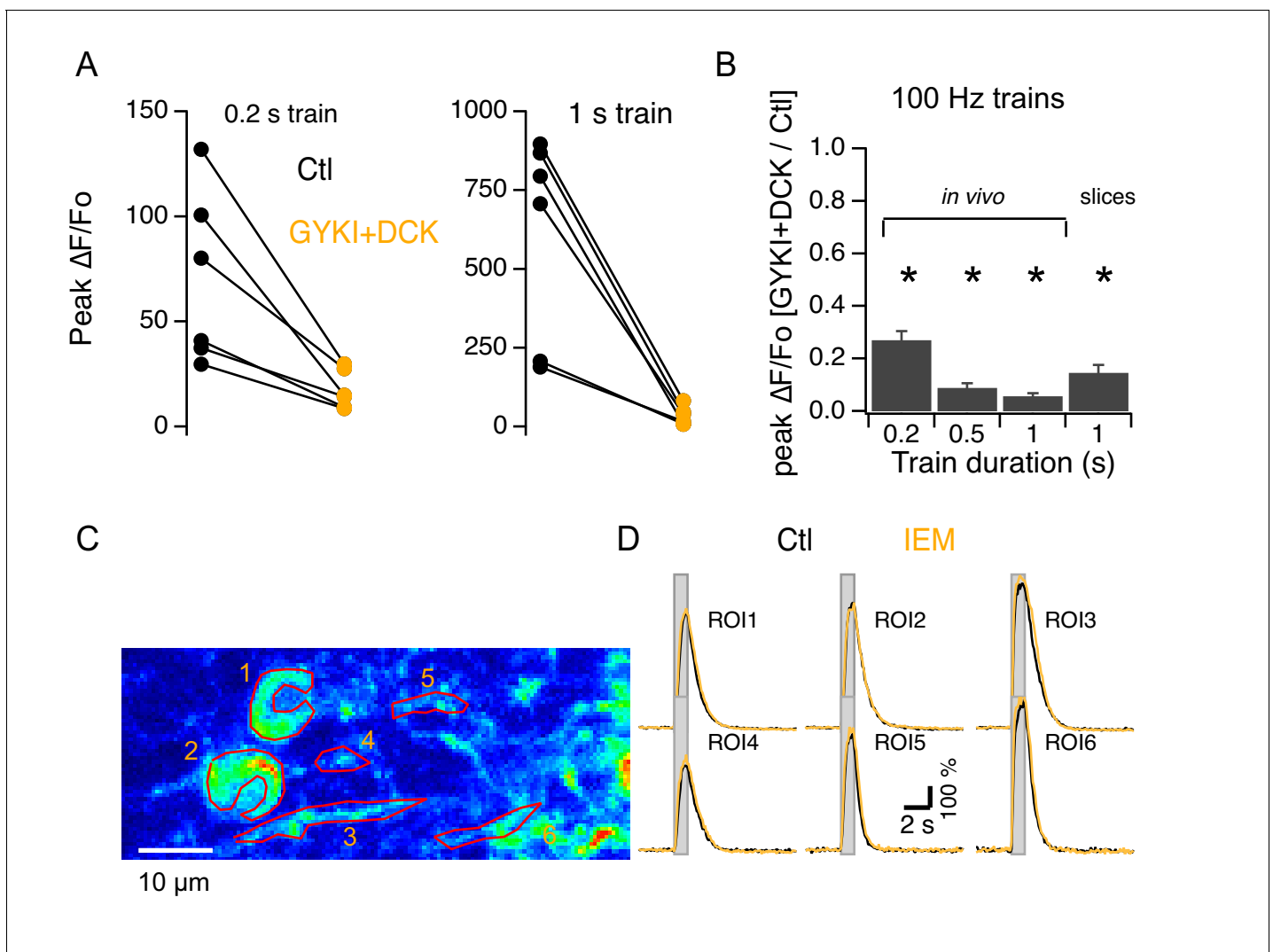


**Figure 4.** Synergy between iGluRs and mGluR1s in adult MLIs. (A) A mixture of 300  $\mu\text{M}$  GYKI53655 and 100  $\mu\text{M}$  DCK blocked somatic  $\text{Ca}_i$  rises under various PF stimulation protocols *in vivo*. (B) Ratios between peak amplitudes of  $\Delta\text{F}/\text{Fo}$  in the blockers over control ( $n = 6$  in each condition). (C,D) GCaMP3 imaging of PF-induced  $\text{Ca}_i$  rises in 2 somata and 4 putative neurites *in vivo* shows no difference between control (black traces) and addition of 40  $\mu\text{M}$  IEM 1460 (yellow traces).

The remaining scenario is AMPA-mediated depolarization recruiting voltage-gated  $\text{Ca}^{2+}$  channels. To test this hypothesis, we investigated the pharmacological properties of  $\text{Ca}_i$  rises elicited by glutamate uncaging in slices. Signals evoked in MLIs by glutamate uncaging had peak  $\Delta\text{F}/\text{Fo}$  values of  $342 \pm 47\%$  ( $n = 12$ ) in control saline and  $5 \pm 3\%$  ( $n = 10$ ) in the presence of CPCCOEt, showing that they were mediated by mGluR1. We found that these  $\text{Ca}_i$  rises were strongly decreased by addition of  $\text{CdCl}_2$  to the extracellular solution (Figure 5C and D). On average, peak  $\Delta\text{F}/\text{Fo}$  decreased from  $438 \pm 47\%$  to  $6 \pm 2\%$  ( $n = 4$ ). These results indicate that iGluRs acts on the mGluR1-induced response via voltage-gated  $\text{Ca}^{2+}$  channels.

### mGluR1 localization at PF-MLIs synapses

We next explored the structural correlates of the mGluR1 signaling with electron microscopy. Using SDS-treated freeze-fracture replica labeling, it has been shown that AMPARs form dense clusters filling the entire area of the postsynaptic density (PSD) at PF-MLI synapses (Masugi-Tokita *et al.*, 2007). Given the dependence of mGluR1s on AMPAR activation, we used the same technique to examine the location of mGluR1s with respect to the PSD. We used an mGluR1 $\alpha$  antibody because



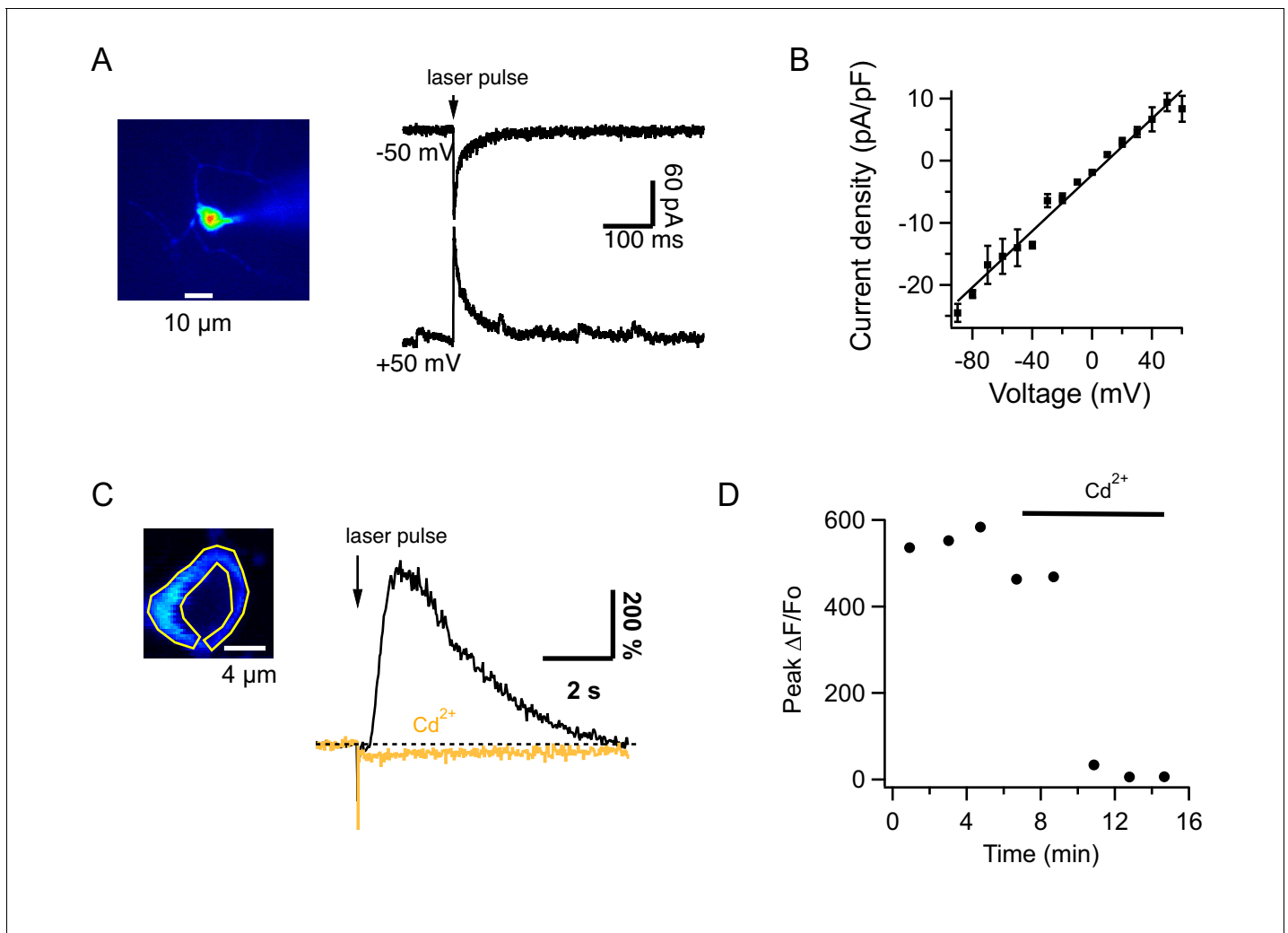


**Figure 5.** Glutamate uncaging from MLIs in slices. (A) MLI currents evoked by MNI-glutamate uncaging in a slice of an adult mouse at different holding potentials in the presence of 100 μM intracellular spermine. (B) The I-V curve from 7 MLIs shows no rectification. (C) *Left:* Image of an MLI expressing GCaMP6s with ROI drawn over the cytosol. *Right:* ΔF/Fo signals evoked by MNI glutamate uncaging in control saline (black) and after addition of 100 μM CdCl<sub>2</sub> to the solution bathing the slice (orange). (D) Temporal evolution of ΔF/Fo signals for the MLI shown in C.

strong mGluR1α immunoreactivity has been described for all GABAergic neurons in the cerebellar cortex (Baude et al., 1993) while no immunoreactivity has been found in MLIs for other mGluR1 isoforms (mGluR1b and mGluR1c) (Grandes et al., 1994). The mGluR1α antibody showed labeling on the P-face of the plasma membrane, whereas no specific labeling was found on the E-face. The MLI dendrites were identified in replica samples by their smooth and thin appearance without spines (Figure 6A). The distance from PSD to each gold particle was measured from mirror replicas with mGluR1α labeling on the P-face and intramembrane particle (IMP) clusters indicating glutamatergic postsynaptic sites on the E-face (Figure 6B). The area of IMP clusters was demarcated manually and copied on the corresponding P-face area, where mGluR1α labeling was detected. From the edge of PSD, 50, 100, 150, 200 and 250 nm distance lines were drawn and the density of mGluR1α particles in these 50 nm-width areas was calculated. This analysis showed that mGluR1α are remarkably close to the PSD, with the highest density occurring within the first 50 nm from the edge of the synapse (Figure 6C). Thus, mGluR1s are ideally located to engage in synergistic interactions with AMPARs following the release of glutamate by presynaptic PFs.

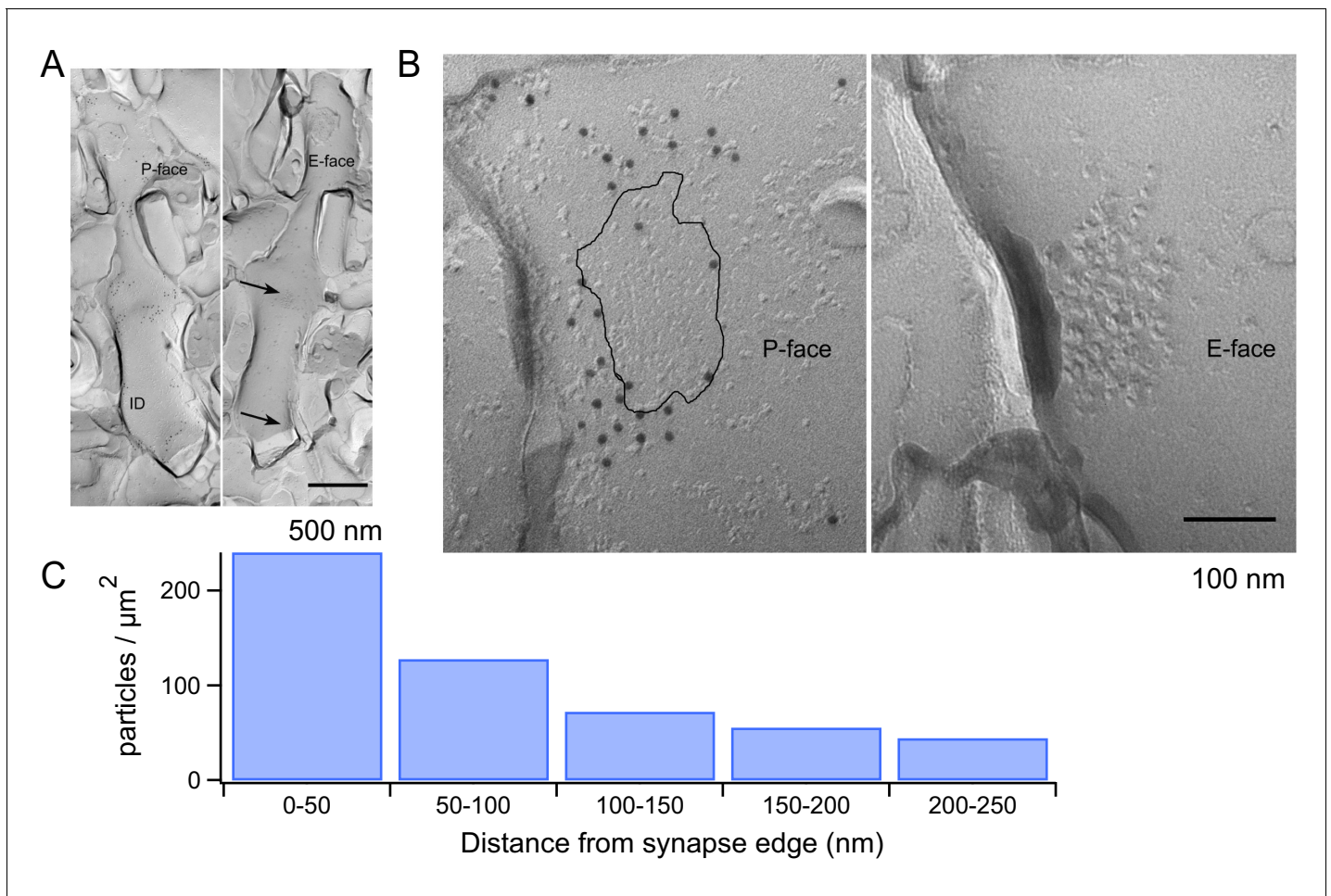


**Figure 6.** mGluR1 distribution at PF-MLI synapses. (A) Low magnification electron micrographs show MLI dendrites in mirror replicas with mGluR1 $\alpha$  labeling (10 nm gold particles) on the protoplasmic face (P-face) and intra-membrane particle clusters (arrows) indicating glutamatergic postsynaptic sites on the exoplasmic face (E-face). Scale bar, 500 nm. (B) Immunogold labeling of freeze-fracture replicas shows mGluR1 $\alpha$  on the P-face concentrated close to the PF-MLI postsynaptic site (black line) identified by intramembrane particle (IMP) clusters on the corresponding E-face. Scale bar, 100 nm. (C) Immunogold particle density as a function of distance from the synapse edge. A similar trend was found in replicas from 2 other animals, in which 241 and 191 particles were analyzed.

## Discussion

Three main findings arise from the present work. Firstly, we show that mGluR1s are activated *in vivo* by synaptically-released glutamate both during electrical stimulation of PFs in anesthetized mice and during enforced locomotion in awake mice. Furthermore, we show that the relative contribution of mGluR1 activation to the postsynaptic  $\text{Ca}_i$  signals increases sharply as a function of the duration of presynaptic action potential trains. Secondly, we show that activation of mGluR1s and iGluRs act in synergy to produce  $\text{Ca}_i$  rises. Third, we show that the spatial distribution of these receptors at the PF-MLI synapse, as revealed by quantitative EM, favors iGluR/mGluR1 synergy following homosynaptic receptor activation.

## Activation of mGluR1s *in vivo*

Given the involvement of mGluR1s in cerebellar processes as diverse as synaptic efficacy (reviews by *Knöpfel and Grandes, 2002; Kano et al., 2008; Hartmann and Konnerth, 2009*), AMPAR  $\text{Ca}^{2+}$  permeability (*Kelly et al., 2009*),  $\text{Ca}^{2+}$  channel activity (*Zheng and Raman, 2011*), synapse elimination (*Uesaka et al., 2014*) and long term synaptic plasticity (*Aiba et al., 1994; Conquet et al., 1994; Welsh et al., 2005*), it is important to determine conditions governing mGluR1 activation *in vivo*.

vivo. MLIs, the neurons of interest in the present study, have long been considered to participate in cerebellar coding through lateral inhibition (Eccles *et al.*, 1966), with recent studies lending further support to this view (Dizon and Khodakhah, 2011). We present here the first evidence for recruitment of mGluR1s on MLIs in vivo. We further show that high frequency trains of PF activity, resembling sensory input to the cerebellar cortex and spike bursts recorded from granule cells (GCs) in vivo during somatosensory peripheral stimulation (Jörntell and Ekerot, 2006), engage mGluR1s depending on the activation of iGluRs. Previous documentation of mGluR1 activation in vivo is very scarce. While mGluR1-dependent  $Ca_i$  signaling has been observed before in vivo following beam activation of PFs (Wang *et al.*, 2011), this signal may have been indirect as it had a latency  $>10$  s; furthermore, its cellular origin remained uncertain, even though it was suggested that the primary signal source was PCs. By contrast, our work indicates direct mGluR1 activation at PF-MLI synapses with a latency well below 1 s. Demonstrating mGluR1 activation at PF-MLI synapses is particularly significant, since in contrast to PF-PC contacts, these synapses lack ensheathing elements that slow neurotransmitter concentration decay and that favor the activation of slowly activating receptors such as mGluR1s. Therefore, our results suggest that mGluR1 activation in vivo may be a widespread phenomenon, occurring under a variety of morphologically different synapses, and following common presynaptic activity patterns.

The activation of MLIs during locomotion reported here is expected as we recorded in lobule IV/V of the cerebellar vermis which encodes fore- and hindlimb sensory-motor information (Provini *et al.*, 1968; Buisseret-Delmas and Angaut, 1993). It is in accord with recent work showing that both electrical activity (Jelitai *et al.*, 2016) and activity-dependent  $Ca_i$  signals in MLIs increase during locomotion (Ozden *et al.*, 2012). How comparable are the two experimental paradigms used in the present work? Although peak  $\Delta F/F_0$  signals are comparable ( $114 \pm 31$  and  $347 \pm 43\%$  for 0.2 and 1 s long trains of electrical stimulation at 100 Hz and  $128.2 \pm 8.5\%$  during locomotion), spatial and temporal patterns of activation differ. Thus, the electrical stimulation we used imposes a 'beam' like pattern of MLI recruitment (with a beam width in the range of 20 to 50  $\mu\text{m}$ ; Figure 1, see also Astorga *et al.*, 2015). On the other hand, locomotion engages a much larger population of MLIs (Figure 3) in accord with results from Ozden *et al.* (2012). Concerning the number of PFs recruited, we presume that action potential thresholds are rather homogeneous across PFs when extracellular stimulation is used, so that all PFs within a beam are excited at the frequency imposed by extracellular stimulation. During locomotion, likewise, a vast majority of GCs are activated, 94% of all GCs in a large field of view, according to Ozden *et al.* (2012) and the impact on MLIs is a change in firing rate from an average value of 20 Hz in quiet mice to 60 Hz during self-paced locomotion (Jelitai *et al.*, 2016). GC firing in mice walking spontaneously is very heterogeneous in time and in space. In time, firing occurs in high frequency bursts with instantaneous frequencies within a burst ranging from 60 to 142 Hz, and burst durations ranging from 30 to 140 ms. Strikingly, these values are close to those needed to obtain measurable mGluR responses with extracellular stimulation (Figure 2). In space, individual GCs are reported to vary markedly in their firing patterns when mice are walking. In view of the results of Figure 3 indicating a measurable mGluR contribution in a rather small proportion of MLIs, it is plausible that particularly active GCs cooperate within the dendritic field of these particular MLIs to produce mGluR activation as a result of temporal and spatial summation of the perisynaptic glutamate concentration.

Our finding that mGluR1 block affects the magnitude of the  $Ca_i$  rises associated with locomotion points to an important role of mGluR1s in cerebellar signal processing during physiologically relevant behaviors. The correlation between the extent of block and the  $Ca_i$  rise amplitude may arise from different patterns of PF activity during the behaviors. Together with our results on PF stimulation, the data from behaving mice aids to generate a picture of mGluR1 activation in the MLIs. During natural behavior, PFs carry sensory codes to the cerebellar cortex where sensory feedback is converted to a well programmed sequence of excitation and inhibition of PCs. MLIs provide the indispensable inhibition (Chu *et al.*, 2012; Jelitai *et al.*, 2016; Gaffield and Christie, 2017; Rowan *et al.*, 2018) and the PF-MLI synapses are the sites controlling the amount of inhibition output (Bao *et al.*, 2010). High frequency or prolonged PF activity will induce strong  $Ca_i$  rises in MLIs through the synergy between iGluRs and mGluR. This synergy works as a nonlinear switch, gating the plasticity at PF-MLI synapses and governing the inhibition output of MLIs.

## Synergistic $\text{Ca}_i$ rises following combined activation of mGluR1s and iGluRs

In slices, the response of MLIs to mGluR1 agonists is abolished by removal of external  $\text{Ca}^{2+}$  ions (Collin *et al.*, 2009) or by inclusion of the VGCC blocker  $\text{Cd}^{2+}$  (this work). This shows that voltage-gated  $\text{Ca}^{2+}$  entry is necessary for mGluR1-activated  $\text{Ca}_i$  rises. In this context, our *in vivo* results showing that mGluR1-dependent rises are totally dependent on simultaneous iGluR activation strongly suggest that AMPAR activation provides a depolarization that activates VGCCs, thus initiating the  $\text{Ca}_i$  rise and bootstrapping the mGluR1-activated response. Although most of our experiments used both AMPAR and NMDAR blockers, the evidence shown in **Figure 2** indicates that AMPARs alone are responsible for the synergy. This is in accordance with the reliance of mGluR1-dependent IP3 production on AMPAR activation at PF-PC synapses (Okubo *et al.*, 2004). A plausible source for the synergistic nature of the signals is the  $\text{Ca}^{2+}$ -dependence of phospholipase C, which has been documented in cerebellar PCs (Kim *et al.*, 2011). Taken together these results suggest that AMPAR/mGluR1 synergy constitutes a double key system controlling postsynaptic  $\text{Ca}_i$  responses following prolonged PF stimulation. This double key control is analogous to the well-documented joined requirement for AMPAR and NMDAR activation in the induction of long-term synaptic plasticity. Interestingly, while NMDARs are present extrasynaptically in MLIs (Carter and Regehr, 2000; Clark and Cull-Candy, 2002), the PF-MLI synapses lack NMDARs (Glitsch and Marty, 1999; Clark and Cull-Candy, 2002). Our data indicates that  $\text{Ca}^{2+}$ -permeable AMPARs are also absent at this synapse. Nevertheless, PF-MLI synapses are the site of various forms of synaptic plasticity (reviewed by Dean *et al.*, 2010). The combined activation of AMPARs and mGluR1s at PF-MLI synapses could control the rise of a postsynaptic calcium signal responsible for associative synaptic plasticity, similarly to the combined activation of AMPARs and NMDARs in other synapses. Likewise, in a subset of interneurons in the hippocampus, a form of long-term synaptic plasticity requires simultaneous activation of mGluR1s, of  $\text{Ca}^{2+}$ -permeant AMPARs, and of T-type  $\text{Ca}^{2+}$  channels (Nicholson and Kullmann, 2017). Interestingly, there is another form of synergy between iGluRs and mGluRs involving the electrical field induced by activation of iGluRs, which retards the escape of charged glutamate from the synaptic cleft and favors the activation of mGluRs (Sylantsev *et al.*, 2013). Our data does not allow us to exclude this possibility, but this phenomenon alone is unlikely to account for the observed synergy, because this synergy depends on  $\text{Ca}^{2+}$  influx.

### Distribution of mGluR1s

It is interesting to compare the mGluR1 $\alpha$  distribution on MLIs and PCs, as these two neuron types share a common presynaptic element but differ regarding the nature of the postsynaptic partner and the morphology of the postsynaptic site. PF-PC synapses are located on PC spines while PF-MLI synapses occur on smooth MLI dendrites. Furthermore, PF-PC synapses are encapsulated with glia, thus preventing neurotransmitter escape, whereas PF-MLI synapses lack ensheathing elements. As in the present work, the location of mGluR1 $\alpha$  on PF-PC synapses was found to be perisynaptic (Baude *et al.*, 1993; Lujan *et al.*, 1996; Luján *et al.*, 1997), and it was calculated that 50% of mGluR1 $\alpha$  particles were located within 60 nm of the edge of the synapse. This percentage is close to the value reported here for MLIs. The close association of mGluR1s with the PSD rim in both synaptic types is consistent with the AMPAR/mGluR1 synergy proposed above. In addition, this spatial arrangement strongly suggests that in both cases, mGluR1 activation primarily results from homosynaptic glutamate release, and not from glutamate spillover. Nevertheless, differences between the two synaptic types are significant. The PSD size for PF-MLI synapses is twice smaller than that of PF-PC synapses (Abrahamsson *et al.*, 2012), and this results in a significantly shorter distance between the site of vesicular release and mGluR1s, favoring homosynaptic activation of mGluR1s. On the other hand, while glial covering and glutamate uptake favor synapse isolation and hence homosynaptic signaling in PF-PC synapses, the absence of a diffusion barrier imposed by glial membranes around the PF-MLI synapse (Palay and Chan-Palay, 1974), and a lower density of glutamate transporter proteins (Chaudhry *et al.*, 1995), would seem to favor activation by synaptic cross-talk in PF-MLI synapses. Nevertheless, the present finding of a close association of mGluR1 to the PSD at PF-MLI synapses suggests that the advantage of the short distance overrules the disadvantage of the lack of glial covering, so that overall, homosynaptic activation prevails also in the case of the PF-MLI synapse.

## Temporal pattern for mGluR1 activation

Compared to AMPARs, mGluR1s display slow activation kinetics and low desensitization rates. Consequently, single synaptic release results in a small number of activated receptors. A few pulses of high frequency release, however, can recruit a sufficient number of mGluR1s to trigger a measurable response as observed in slice experiments for PF-PC synapses (Finch and Augustine, 1998; Takechi et al., 1998) and for PF-MLI synapses (Karakossian and Otis, 2004). Longer stimulation trains are expected to recruit an increasing proportion of mGluR1s as their activation develops further while AMPAR desensitization occurs. Our in vivo results are in line with this expectation, showing a growing contribution of mGluR1s to PF-induced  $Ca_i$  responses as a function of train duration. We start seeing mGluR1-mediated  $Ca_i$  rises for bursts of PF activity lasting about 100 ms, a duration commonly recorded in vivo during sensory input or behavior (Jörntell and Ekerot, 2006). Given the above slice results, and because our GCaMP-based signals do not have the same resolution as signals reported by organic  $Ca^{2+}$  dyes, it is probable that the actual threshold for activation of mGluR1 in vivo is somewhat lower than our 100 ms estimate.

## Materials and methods

Experimental procedures complied with animal care guidelines of the University Paris Descartes and the guidelines of the Animal Care and Use committee of University of Science and Technology of China. Experimental procedures were approved by the 'Prefecture de Police' (#A-750607) in agreement with the European Directive 86/609/EEC and by the ethical committee of the University Paris Descartes.

Estimation of sample size was according to published in vivo and in vitro work. Sample size for each experiment is indicated in the main text.

## GCaMP expression in the cerebellar cortex

4–5 weeks old female mice heterozygous for an allele driving cre recombinase under the control of the PV promoter (Hippenmeyer et al., 2005), *Pvalb-Cre* mice, were deeply anesthetized with intraperitoneal injection of ketamine (14.8  $\mu$ g/g)/xylane (10  $\mu$ g/g) and mounted in a stereotaxic frame. A midline sagittal incision exposed the cranium over the cerebellar vermis. At the site of injection (6 mm from Bregma and 0.6 mm lateral) a 0.5 mm burr hole was drilled and a 34-gauge stainless steel beveled needle (WPI-nanofil) was slowly descended 0.4 mm through a slit cut in the meninges. After a 2 min pause, the needle was retracted 50  $\mu$ m and then 1.2  $\mu$ l of AAV2/1.hSyn.Flex.GCaMP3.WPRE.SV40, AAV2/9.hSyn.Flex.GCaMP3.WPRE.SV40 (Tian et al., 2009) or AAV2/1.hSyn.Flex.GCaMP5G.WPRE.SV40 (Akerboom et al., 2012) were injected at a rate of 0.1  $\mu$ l/min. Viral constructs were purchased from the University of Pennsylvania Vector Core service. Once completed, the needle was left in place an additional 10 min before being withdrawn, the scalp sutured, and the mouse kept under a warming lamp until recovered from the anesthesia before finally being returned to standard housing.

## GCaMP imaging in anesthetized mice

2 to 4 weeks after stereotaxic vector delivery, mice were prepared for imaging as described in detail previously (Franconville et al., 2011). The time of expression was chosen to avoid GCaMP overexpression (Tian et al., 2009; Zariwala et al., 2012). In some sections, as indicated in the text, data was pooled from mice expressing GCaMP3 and GCaMP5G, since these proteins have similar  $Ca^{2+}$  affinities and kinetic parameters (Akerboom et al., 2012). During imaging anesthesia was delivered via an intraperitoneal catheter and vital parameters were continuously monitored using a Pulse Oxymeter system (Starr Life Sciences, USA). 2-photon laser scanning imaging was performed with a custom-built set-up (details in Franconville et al., 2011). Excitation wavelength was 910 nm. Imaging depth ranged from 50 to 100  $\mu$ m from the surface, thus excluding basket cells.

Extracellular electrical stimulation was delivered through a theta-glass pipette filled with a HEPES-buffered extracellular saline to which 20  $\mu$ M Alexa 594 dye was added to aid visualization. The pipette was placed on the superficial molecular layer more than 150  $\mu$ m from the site imaged to avoid direct stimulation of the neurons in that field. Ag-AgCl electrodes connected the pipette to an isolated pulse stimulator (AM-systems) delivering 200  $\mu$ s long pulses at 30–80 V amplitude. Initial

search for stimulation site and parameters was performed with the criteria that 10 pulses at 100 Hz elicited  $Ca_i$  rises whose trial-to-trial variability did not exceed 10%. The number of repetitions and stimulation strength were kept to a minimum in order to limit activity-dependent changes in AMPAR function (Cull-Candy *et al.*, 2006).

Glutamate receptor antagonists GYKI 53655, 5,7-Dichlorokynurenic acid (DCK), CPCCOEt and IEM 1460 were purchased from Tocris or Accent Scientific. Drugs were added to the artificial cerebrospinal fluid solution (ACSF) on the pool bathing the cranial window, which had the following composition (in mM): 150 NaCl, 2.5 KCl, 1 MgCl<sub>2</sub>, 1.5 CaCl<sub>2</sub>, 10 Hepes, adjusted to a pH of 7.3 with 1 M NaOH solution).

### GCaMP imaging in slices

One to three weeks after stereotaxic injection, sagittal cerebellar slices were prepared in sucrose-containing saline as described previously (Franconville *et al.*, 2011) or using a low Na<sup>+</sup> saline designed for slicing of adult mice brain (Zhao *et al.*, 2011) with the following composition (in mM): 93 N-methyl-D-glucamine, 2.5 KCl, 1.25 NaH<sub>2</sub>PO<sub>4</sub>, 25 NaHCO<sub>3</sub>, 0.5 CaCl<sub>2</sub>, 10 MgCl<sub>2</sub>, 20 Hepes, 5 Na ascorbate, 2 thiourea, 3 Na pyruvate and 25 glucose (HCl added to bring pH to 7.4). Slices were maintained for 30–40 min at 34°C in standard recording saline (in mM: 125 NaCl, 2.5 KCl, 1.25 NaH<sub>2</sub>PO<sub>4</sub>, 25 NaHCO<sub>3</sub>, 2 CaCl<sub>2</sub>, 1 MgCl<sub>2</sub>, and 10 glucose) prior to transfer to the recording set-up. 2PLS imaging was performed at 34°C using an excitation wavelength of 910 nm. Even though precautions were taken to optimize slice survival, a variable fraction of MLIs displayed nuclear fluorescence after slicing. At equivalent expression times, nuclear fluorescence was not observed in vivo, suggesting that changes in the subcellular distribution of the GCaMP protein are due to the slicing procedure. Such changes are indicative of deleterious effects of slicing and therefore emphasize the importance of in vivo studies. MLIs were studied only if their nucleus did not show any fluorescence. Imaging was performed at depths of 40 to 70 μm from the slice surface. Imaging and extracellular stimulation were as described in Collin *et al.* (2009) and references within.

### Glutamate photorelease in slices

For whole-cell recording (WCR) experiments, slices from mice aged 30–35 days were prepared as described above. Extracellular recording saline contained (in mM): 135 NaCl, 4 KCl, 2 NaHCO<sub>3</sub>, 25 glucose, 2 CaCl<sub>2</sub>, 0.1 MgCl<sub>2</sub> and 10 HEPES, pH 7.4 with NaOH. WCR was performed in MLIs with an intracellular solution containing (in mM): 140 Cs Gluconate, 4 MgCl<sub>2</sub>, 10 HEPES-K, 0.4 Na-GTP, 4 Na-ATP and 100 μM spermine, pH 7.3 with CsOH. MNI-glutamate (0.9 mM) was added to the recording chamber and photolysis was achieved with 100 μs pulses from a 405 nm laser as described elsewhere (Rossi *et al.*, 2008). Currents evoked by MNI photolysis were recorded at holding potentials ranging from –100 to 80 mV. To study effects of Cd<sup>2+</sup> on glutamate uncaging-evoked  $Ca_i$  signals, we prepared slices from transgenic animals (PN30-45) issued from a cross of mice carrying the GCaMP6f transgene in the *Igs7* locus (Jackson labs stock number 024107) and *Pvalb-Cre* mice. Expression pattern was similar to that obtained with viral injections.

### Experimental design and data analysis for anesthetized and in vitro imaging

In vivo experiments were usually performed 2–3 days in a row in a week depending on the availability of the transgenic mice and the success of viral injection. In each animal, all activated neurons within the focal plane were sampled. Biological replicates were the number of animals used in the experiments. Technical replicates were the number of repeated stimulations for each condition. Outliers were not excluded from the data pool.

Data were analyzed with custom-written routines in Igor Pro (Wavemetrics). Background fluorescence  $F_b(t)$  was estimated as the average fluorescence of 20–30 pixels with the lowest F value throughout all the frames of the sequence. A somatic ROI was defined by a polygon drawn along the contour of the ring-shaped somatic pre-stimulus fluorescence.  $F(t)$  was calculated as the time course of the averaged fluorescence from all pixels in a ROI.  $\Delta F/F_0$  was computed as  $(F(t)-F_0)/(F_0-F_B)$ .  $F_0$  and  $F_B$  are the averages of  $F(t)$  and  $F_b(t)$  over the pre-stimulus period respectively. Values for pooled data are given as mean ± s.e.m. When assessing drug effects, results from GCaMP3 and GCaMP5 were pooled together, because these two GECLs have similar affinities for Ca<sup>2+</sup>

(Akerboom *et al.*, 2012). For statistical analysis, we applied non-parametric two-tailed Wilcoxon signed test to test the null hypothesis based on the fact that data points were from different cells and their peak calcium transients should not follow a normal distribution. All the statistical information is indicated in the main text or figure legends. Groups were considered significantly different for  $p \leq 0.05$ .

## GCaMP imaging in behaving mice

### Chronic window and head-plate surgery

Three weeks after stereotaxic injection, mice were prepared for imaging during locomotion by implanting a chronic window and fixing a head post. Before surgery (10–15 min), mice were injected with buprenorphine (0.35 mg/kg intraperitoneal) for pain reduction. Lidocaine was used as a local anesthetic. Surgeries were performed under isoflurane (1.5–2.0% by volume in air) to maintain a surgical plane of anesthesia as determined by non-responsiveness to toe pinch. Eye ointment was applied under anesthesia at the start of surgery. Animals were held in a stereotaxic apparatus using ear and nose bars to stabilize the head. Body temperature was set with a heating pad and controller using biofeedback from a rectal thermocouple.

For the surgical procedure, the area of the head over the cerebellum was first shaved and the underlying skin was treated repeatedly with ethanol (70%) and Betadine in alternation. The skin above the skull was removed and the opening of the periosteum as well as any membranous tissue were cleaned. Once the skull was dry, a cranial window was carefully drilled using a handheld high-speed micromotor drill (Freedom). The center of the craniotomy was located ~2 mm from lambda on the midline targeting lobule IV/V of the cerebellar vermis. Skull removal was performed under application of an ACSF solution to minimize the risk of damaging the dura overlying the brain. After skull removal, the ACSF solution was used to clean any debris from the brain surface and to maintain the brain moist providing an interface to the chronic window. A chronic window was fabricated from a cover glass (#1, thickness 150  $\mu\text{m}$ ) laser cut to a small oval shape (2.5 mm x 2 mm) to better fit the cranial opening, and to feature two holes of ~500  $\mu\text{m}$  diameter and 1.5 mm separation on the major axis for drug delivery. The window was placed over the cerebellar vermis lobule IV/V and kept in direct contact with the brain by lowering the window with the help of a needle mounted in the stereotaxic setup. The chronic window was fixed in place with dental cement (Super-Bond C and B). After setting of the dental cement, the bone surrounding the craniotomy was thinned with the micromotor drill to allow for better access with the 20x objective. Then a custom-made stainless steel head post with a central opening for the craniotomy was cemented in place with dental cement (Super-Bond C and B). The chronic window was covered with silicone for protective purposes after surgery. Mice were carefully monitored during surgical recovery, with all animals showing normal behavior including the absence of motor deficits. Mice were allowed to recover at least 2 days before proceeding to the locomotion and imaging experiments with ad libitum access to food and water.

### Fluorescence imaging during forced locomotion in awake mice

A sketch of the imaging setup can be seen in **Figure 3A**. For our experimental recordings and manipulations, mice were manually placed in a purpose-built apparatus by attaching the surgically implanted head post to a rigid fixture. Mice were positioned with the tip of the nose ~5 mm above the spherical treadmill, and with an angle of ~10° between the tangent of the treadmill and the bottom of the lower jaw, a position which was inferred from free walking on the treadmill. The treadmill's surface was covered with a plastic mesh (square grid of 5 × 5 mm) allowing for easy grip. Mice could walk self-paced on the treadmill. 2-photon laser scanning imaging was performed in the medial part of lobule IV/V of the cerebellar vermis region with a custom-built setup (for details, see **Franconville *et al.*, 2011**), which was extended with a resonant scanning mirror (Sutter ResScan-Gen). Imaging was performed in the molecular layer at depths of 50 to 100  $\mu\text{m}$  from the surface and the field of view was chosen in order to maximize the number of simultaneously recorded MLI somata. Excitation wavelength of the laser (MaiTai, Spectra Physics) was set at 910 nm and in some cases to 820 nm to measure movement related fluorescent changes. Laser power out of the objective (20x, 1.0 NA, Olympus, XLUMPlanFI N) was typically <80 mW. The photodetector was a photomultiplier tube (Hamamatsu, H7422P-40MOD) placed proximal to the imaging plane to maximize

photon collection. Sequences of images were acquired at 30 Hz and comprised a  $400 \times 400 \mu\text{m}$  field of view with a pixel size of  $0.78 \times 0.78 \mu\text{m}$  using the ScanImage 2015 software (Pologruto *et al.*, 2003).

Imaging recordings lasted for 40 s and were repeated every 2–4 min. The speed and the duration of locomotion during the recordings was imposed in an attempt to minimize variations across recordings. The forced locomotion scheme was as follows: Recordings started with a 6 s long period of baseline during which the mouse was able to freely rotate the treadmill. At 6 s, a servo motor moved a continuous rotation servo in a gear attached to the axis of the treadmill. The continuous servo started to linearly accelerate ( $3.33 \text{ cm/s}^2$ ) the wheel at 7 s until a maximal speed of 10 cm/s was reached at 10 s. This rotation speed was kept constant until 23 s at which point the motor linearly decelerated ( $-3.33 \text{ cm/s}^2$ ) until standstill at 26 s and then moved out of the gear on the treadmill axis allowing for self-paced walking. The rotation of the treadmill was recorded with a rotary encoder (Pewatron, E7P-700-315-D-D-D-3) at 40 kHz with a standard DAQ acquisition board (National Instruments, PCIe 6323). Mice were monitored with infra-red (940 nm LED illumination) videography at 200 frames/s (camera: Dalsa Genie Nano, NANO-M800-NIR) during the entire recording sessions.

### Pharmacology in behaving mice

After recording baseline fluorescence during forced locomotion, the craniotomy bath ACSF solution (see composition above) was exchanged with a ACSF containing additionally 100 (animal #1A, #3) or 200  $\mu\text{M}$  CPCCOEt (animal #1, #2, #4). Two holes of  $\sim 500 \mu\text{m}$  diameter were drilled in the cover-slips prior to implantation to allow for drug access. To further improve drug access, the dura mater was pierced with a sharp glass pipette before the experiment under anesthesia (1.5% isoflurane in air). In a subset of experiments (4 out of 5 recordings), 50  $\mu\text{M}$  Alexa 594 was added to the drug-containing ACSF to assess the dynamics of drug diffusion in the recorded brain area (Figure 3—figure supplement 1). 50  $\mu\text{M}$  Alexa 594 was added to bath ACSF after the locomotion recordings with CPCCOEt in animals #1A.

Fluorescence recordings during forced-locomotion before- and after drug application were performed in 4 mice in total. One of the animals was recorded on two different days (animal#1A, animal#1). The first recording of animal #1, animal#1A, was removed from all further analysis based on the lack of fast Alexa fluorescence increase (Figure 3—figure supplement 1). The four remaining recordings from four different animals (#1,#2,#3,#4) were treated independently in the analysis described below.

### Calcium imaging processing

The pre-processing of all raw calcium imaging data – image registration and ROI detection – was done using Suite2p using default settings (Pachitariu *et al.*, 2007). ROI identity was furthermore visually verified and corrected when necessary for all recordings, that is, only ROIs spatially restricted to MLI somata were included in subsequent analysis. Subsequent image analysis was implemented using custom routines written in the Python programming language. Image stacks recorded before and after drug application were aligned using rigid translation through Enhanced Correlation Coefficient Maximization (Evangelidis and Psarakis, 2008) implemented in the OpenCV package for Python. Alignment was necessary since the application of the drug required removal of the objective which involved microscope stage movements. ROIs were aligned according to this translation and were considered to comprise the same soma if the overlap between the ROI areas before and after drug application was at least 30% of the total combined ROI area, that is,  $0.3 \leq A_{\text{overlap}}/A_{\text{union}}$  with  $A_{\text{overlap}} = A_{\text{before drug}} \cap A_{\text{after drug}}$  and  $A_{\text{union}} = A_{\text{before drug}} \cup A_{\text{after drug}}$ . The fluorescent traces of overlapping ROIs were then compared between the before and after drug condition.

Cellular fluorescence traces were first compensated for surrounding neuropil signal by subtracting a scaled-down version, that is,  $F^{i,j} = F^{i,j}_{\text{MLI}} - 0.7 F^{i,j}_{\text{Neuropil}}$  ( $i$  denotes all identified ROIs, and  $j$  refers to the recording number). Subsequently, fluorescence traces were normalized using the pre-motorization baseline period ( $< 5$  s). Blocks of recordings were scanned for a recording  $j = k$  with the least active baseline period based on the rotary encoder recordings, that is, the recording  $j = k$  for which the animal showed the least amount of locomotor activity during the first 5 s. Fluorescence during that least active baseline, referred to as  $F_{\text{rest}}$ , was averaged for each ROI following



$F_{rest}^i = \langle F^{i,j=k}(t)_{\text{least active baseline}} \rangle_{t \in [0,5]}$ , where  $i$  denotes the index of the respective ROI and brackets  $\langle \rangle$  indicate the temporal averaging. ROI fluorescence traces of a block of recordings  $j$  were then normalized using this baseline activity according to  $\Delta F^{i,j}/F_{rest}^i = (F^{i,j} - F_{rest}^i)/F_{rest}^i$ .

In order to study locomotion-linked fluorescence, we calculated the 75<sup>th</sup> percentile of  $\Delta F^{i,j}/F_{rest}^i$  during the maximal-speed motorization period  $t \in [10,25]$  s. When using the 75<sup>th</sup> percentile, the fluorescence values of the drops of fluorescence during locomotion (see **Figure 3C**) do not affect the analysis. Rather, the 75<sup>th</sup> percentile emphasizes the high fluorescence parts on which we want to focus here. We observed an overall decay of locomotion fluorescence with increasing number of repetitions, which was shared across all ROIs (see **Figure 3E**). In order to compensate for that decay, we fitted a single-exponentially decaying function  $f(j) = A + B e^{-j/C}$  (where  $j$  denotes pre-drug recording numbers as linearly increasing integers; A, B, C are fit parameters) to the *pre-drug* locomotion fluorescence values. This function is subtracted from *all* recordings, pre- and after-drug, which normalized the pre-drug locomotion fluorescence to zero and revealed any drug induced change beyond the general decay (see **Figure 3F**). Note that by considering the decay as function of recordings  $j$ , the fluorescence decay is linked to the increasing number of the recordings rather than explicit time.

To test for changes in drug-induced fluorescence, we performed paired t-test comparisons for each ROI between all pre- and post-drug locomotion fluorescence values (see **Figure 3**) excluding the first three recordings after drug-delivery to account for the wash-in time of the drug ( $\tau = 5.5$  min, see **Figure 3—figure supplement 1**).

To assess fluorescence changes linked to calcium vs. changes related to movement artifacts in the recorded tissue, we performed forced locomotion recordings before application of CPCCOEt at 820 nm laser excitation wavelength at which GCaMP fluorescence is insensitive to the calcium changes (see **Figure 3—figure supplement 2**). The calcium imaging recordings went through the same image processing procedure as outlined above for the 910 nm excitation wavelength recordings. However, ROI detection was impaired in Suite2p due to the strongly reduced temporal ROI fluorescence dynamics. ROIs corresponding to MLI cell bodies were therefore mostly labeled by hand using oval shapes. Fluorescence images from before drug application and 820 nm excitation runs were aligned (see above). ROIs with an overlap of at least 30% of the total ROI area were considered corresponding to the same cell body (see above). The standard deviation and 75<sup>th</sup> percentile of the  $\Delta F^{i,j}/F_{rest}^i$  were calculated for the maximal-speed locomotion period ([10,25] s). The same values were extracted for the corresponding ROIs from the runs before drug application and averaged. **Figure 3** summarizes the ratios between the 820 and the 910 nm excitation wavelength runs of all ROIs per animal. A fraction of 30–50% of the fluorescence changes can be attributed to movement artifacts (**Figure 3—figure supplement 2A**), while the increase in fluorescence is largely driven by calcium (**Figure 3—figure supplement 2B**). The calcium-associated increase in fluorescence is the focus of the here presented analysis.

All analysis scripts are available online (**Graupner, 2020**; copy archived at [https://github.com/elifesciences-publications/mGluR\\_MLI\\_in-vivo](https://github.com/elifesciences-publications/mGluR_MLI_in-vivo)).

## Immunocytochemistry

Mice were anesthetized by intraperitoneal injection of sodium pentobarbital (Roche) and transcardially perfused by cold Phosphate Buffer Saline (PBS) followed by PBS containing 4% of paraformaldehyde (PFA). After decapitation the cerebellum was removed and post fixed in PBS PFA solution for 2 hr. 50  $\mu\text{m}$  thick parasagittal slices were prepared from the vermis using a vibrating slicer (Leica VT 1000S, Leica Microsystems, Germany). The slices were first incubated in PBS containing 0.3% Triton and 10% fetal bovine serum for 5 hr at room temperature then at 4°C overnight with a mixture of rabbit polyclonal serum anti-Parvalbumin (PV25, SWANT, Marly, Switzerland) and guinea pig polyclonal serum anti calbindin D28k (Synaptic Systems, Göttingen, Germany) diluted to 1/1000 in PBS containing 1 mg/ml of Bovine Serum Albumine (BSA). After 3 washes in PBS, the slices were incubated for 3 hr with secondary goat antibodies anti-rabbit IgG and anti-guinea pig IgG conjugated to Alexa fluor 546 and Alexa fluor 647 respectively (1/500, Molecular Probes, Eugene, OR). Slices were mounted between slides and cover slip with Vectashield Mounting Medium (Vector lab, Burlingame, CA). Stack of images (0.44  $\mu\text{m}$  thickness) were acquired using an LSM 510 confocal microscope (Zeiss, Jena, Germany) equipped with Plan-Neofluar 40x/1.3 oil objective and appropriate excitation

(488, 543 and 633 nm) and emission filters (BP 505–530, BP560\_615 and LP 650). Image analysis and projections were done by LSM and ImageJ Software.

### SDS-digested freeze-fracture replica labeling (SDS-FRL)

SDS-FRL was performed as described previously (*Masugi-Tokita et al., 2007*). Adult Wistar rats were perfused transcardially with 2% paraformaldehyde (PFA) and 15% saturated picric acid solution in 0.1 M phosphate buffer (PB). Sagittal slices (130  $\mu$ m thick) were cut from middle cerebellar lobules and trimmed slices containing molecular layer were rapidly frozen by a high-pressure freezing machine (HPM010, BAL-TEC, Balzers), fractured into two parts at  $-140^{\circ}\text{C}$ , and replicated by a freeze-fracture replica machine (JFD II, JEOL, Tokyo). Tissue debris was dissolved with gentle shaking at  $80^{\circ}\text{C}$  for 18 hr in a solution containing 15 mM Tris-HCl (pH 8.3), 20% sucrose, and 2.5% SDS. The replicas were reacted with rabbit anti-mGluR1 $\alpha$  antibody (*Shigemoto et al., 1997*) (1:500 dilution) followed by anti-rabbit secondary antibody conjugated with 10 nm gold particles (British Biocell International, BBI, Cardiff). The specificity of freeze-fracture replica labeling for mGluR1 was verified using mGluR1 KO mice, as shown in *Mansouri et al., 2015*. The labeled replicas were examined using a transmission electron microscope (JEM 1010, JEOL, Tokyo).

### Acknowledgements

This work was supported by the ‘Agence Nationale de la Recherche’ (projects INNET: ANR-11BSV401001 and REWINHIB: ANR-18-CE16-0010-01), a NeRF postdoctoral fellowship to G Astorga, a Marie Curie Intra European Fellowship to J Bao, and research grants from the National Natural Science Foundation of China (31571073, 81401025) to J Bao. We acknowledge the use of the animal rearing service of the BioMedTech Facilities (INSERM US36, CNRS UMS2009, Université de Paris). We thank L Looger, J Akerboom and DS Kim from the GENIE Project, Janelia Farm Research Campus, for making available the GCaMP3 and GCaMP5 plasmids. We thank J Sheng from University of Science and Technology of China for help in illustration. We thank A Marty for comments on the manuscript.

### Additional information

#### Funding

| Funder                                       | Grant reference number                                     | Author            |
|--|--|-------------------|
| Agence Nationale de la Recherche             | ANR-11BSV401001  | Isabel Llano      |
| Agence Nationale de la Recherche             | ANR-18-CE16-0010-01  | Isabel Llano      |
| European Commission                          | Marie Curie Intra European Fellowship, grant number 302819 | Jin Bao           |
| National Natural Science Foundation of China | 31571073   | Jin Bao           |
| National Natural Science Foundation of China | 81401025   | Jin Bao           |
| NeRF postdoctoral fellowship                 |  | Guadalupe Astorga |

The funders had no role in study design, data collection and interpretation, or the decision to submit the work for publication.

#### Author contributions

Jin Bao, Michael Graupner, Conceptualization, Software, Formal analysis, Investigation, Methodology, Writing - review and editing; Guadalupe Astorga, Investigation, Writing - review and editing; Thibault Collin, Conceptualization, Formal analysis, Investigation, Writing - review and editing; Abdellali Jalil, Dwi Wahyu Indriati, Formal analysis, Investigation, Writing - review and editing; Jonathan Bradley, Conceptualization, Investigation, Methodology, Writing - review and editing; Ryuichi

Shigemoto, Conceptualization, Formal analysis, Funding acquisition, Investigation, Methodology, Writing - review and editing; Isabel Llano, Conceptualization, Formal analysis, Funding acquisition, Investigation, Methodology, Writing - original draft, Project administration, Writing - review and editing

#### Author ORCIDs

Jin Bao  <http://orcid.org/0000-0003-1234-5578>

Michael Graupner  <https://orcid.org/0000-0002-1197-2388>

Jonathan Bradley  <http://orcid.org/0000-0002-6933-1153>

Ryuichi Shigemoto  <http://orcid.org/0000-0001-8761-9444>

Isabel Llano  <https://orcid.org/0000-0002-7217-9711>

#### Ethics

Animal experimentation: Experimental procedures complied with animal care guidelines of the University Paris Descartes and the guidelines of the Animal Care and Use committee of University of Science and Technology of China. Experimental procedures were approved by the "Prefecture de Police" (#A-750607) in agreement with the European Directive 86/609/EEC and by the ethical committee of the University Paris Descartes.

#### Decision letter and Author response

Decision letter <https://doi.org/10.7554/eLife.56839.sa1>

Author response <https://doi.org/10.7554/eLife.56839.sa2>

---

## Additional files

### Supplementary files

- Transparent reporting form

### Data availability

All data generated or analysed during this study are included in the manuscript and supporting files.

---

## References

- Abrahamsson T, Cathala L, Matsui K, Shigemoto R, Digregorio DA. 2012. Thin dendrites of cerebellar interneurons confer sublinear synaptic integration and a gradient of short-term plasticity. *Neuron* **73**:1159–1172. DOI: <https://doi.org/10.1016/j.neuron.2012.01.027>, PMID: 22445343
- Aiba A, Kano M, Chen C, Stanton ME, Fox GD, Herrup K, Zwingman TA, Tonegawa S. 1994. Deficient cerebellar long-term depression and impaired motor learning in mGluR1 mutant mice. *Cell* **79**:377–388. PMID: 7954803
- Akerboom J, Chen TW, Wardill TJ, Tian L, Marvin JS, Mutlu S, Calderón NC, Esposti F, Borghuis BG, Sun XR, Gordus A, Orger MB, Portugues R, Engert F, Macklin JJ, Filosa A, Aggarwal A, Kerr RA, Takagi R, Kracun S, et al. 2012. Optimization of a GCaMP calcium Indicator for neural activity imaging. *Journal of Neuroscience* **32**:13819–13840. DOI: <https://doi.org/10.1523/JNEUROSCI.2601-12.2012>, PMID: 23035093
- Astorga G, Bao J, Marty A, Augustine GJ, Franconville R, Jalil A, Bradley J, Llano I. 2015. An excitatory GABA loop operating in vivo. *Frontiers in Cellular Neuroscience* **9**:275. DOI: <https://doi.org/10.3389/fncel.2015.00275>, PMID: 26236197
- Astorga G, Li D, Therreau L, Kassa M, Marty A, Llano I. 2017. Concerted interneuron activity in the cerebellar molecular layer during rhythmic oromotor behaviors. *The Journal of Neuroscience* **37**:11455–11468. DOI: <https://doi.org/10.1523/JNEUROSCI.1091-17.2017>, PMID: 29066561
- Bak IJ, Misgeld U, Weiler M, Morgan E. 1980. The preservation of nerve cells in rat neostriatal slices maintained in vitro: a morphological study. *Brain Research* **197**:341–353. DOI: [https://doi.org/10.1016/0006-8993\(80\)91120-8](https://doi.org/10.1016/0006-8993(80)91120-8), PMID: 6250666
- Bao J, Reim K, Sakaba T. 2010. Target-dependent feedforward inhibition mediated by short-term synaptic plasticity in the cerebellum. *Journal of Neuroscience* **30**:8171–8179. DOI: <https://doi.org/10.1523/JNEUROSCI.0276-10.2010>, PMID: 20554867
- Baude A, Nusser Z, Roberts JD, Mulvihill E, Mclhinney RA, Somogyi P. 1993. The metabotropic glutamate receptor (mGluR1 alpha) is concentrated at Perisynaptic membrane of neuronal subpopulations as detected by immunogold reaction. *Neuron* **11**:771–787. DOI: [https://doi.org/10.1016/0896-6273\(93\)90086-7](https://doi.org/10.1016/0896-6273(93)90086-7), PMID: 8104433

- Buisseret-Delmas C**, Angaut P. 1993. The cerebellar olivo-corticonuclear connections in the rat. *Progress in Neurobiology* **40**:63–87. DOI: [https://doi.org/10.1016/0301-0082\(93\)90048-W](https://doi.org/10.1016/0301-0082(93)90048-W), PMID: 8424128
- Carter AG**, Regehr WG. 2000. Prolonged synaptic currents and glutamate spillover at the parallel fiber to stellate cell synapse. *The Journal of Neuroscience* **20**:4423–4434. DOI: <https://doi.org/10.1523/JNEUROSCI.20-12-04423.2000>
- Chaudhry FA**, Lehre KP, van Lookeren Campagne M, Ottersen OP, Danbolt NC, Storm-Mathisen J. 1995. Glutamate transporters in glial plasma membranes: highly differentiated localizations revealed by quantitative ultrastructural immunocytochemistry. *Neuron* **15**:711–720. DOI: [https://doi.org/10.1016/0896-6273\(95\)90158-2](https://doi.org/10.1016/0896-6273(95)90158-2), PMID: 7546749
- Chu CP**, Bing YH, Liu H, Qiu DL. 2012. Roles of molecular layer interneurons in sensory information processing in mouse cerebellar cortex crus II in vivo. *PLOS ONE* **7**:e37031. DOI: <https://doi.org/10.1371/journal.pone.0037031>, PMID: 22623975
- Clark BA**, Cull-Candy SG. 2002. Activity-dependent recruitment of extrasynaptic NMDA receptor activation at an AMPA receptor-only synapse. *The Journal of Neuroscience* **22**:4428–4436. DOI: <https://doi.org/10.1523/JNEUROSCI.22-11-04428.2002>, PMID: 12040050
- Collin T**, Franconville R, Ehrlich BE, Llano I. 2009. Activation of metabotropic glutamate receptors induces periodic burst firing and concomitant cytosolic Ca<sup>2+</sup> oscillations in cerebellar interneurons. *Journal of Neuroscience* **29**:9281–9291. DOI: <https://doi.org/10.1523/JNEUROSCI.1865-09.2009>, PMID: 19625518
- Conquet F**, Bashir ZI, Davies CH, Daniel H, Ferraguti F, Bordi F, Franz-Bacon K, Reggiani A, Matarese V, Condé F. 1994. Motor deficit and impairment of synaptic plasticity in mice lacking mGluR1. *Nature* **372**:237–243. DOI: <https://doi.org/10.1038/372237a0>, PMID: 7969468
- Cull-Candy S**, Kelly L, Farrant M. 2006. Regulation of Ca<sup>2+</sup>-permeable AMPA receptors: synaptic plasticity and beyond. *Current Opinion in Neurobiology* **16**:288–297. DOI: <https://doi.org/10.1016/j.conb.2006.05.012>, PMID: 16713244
- Dean P**, Porrill J, Ekerot C-F, Jörntell H. 2010. The cerebellar microcircuit as an adaptive filter: experimental and computational evidence. *Nature Reviews Neuroscience* **11**:30–43. DOI: <https://doi.org/10.1038/nrn2756>
- Dizon MJ**, Khodakhah K. 2011. The role of interneurons in shaping purkinje cell responses in the cerebellar cortex. *Journal of Neuroscience* **31**:10463–10473. DOI: <https://doi.org/10.1523/JNEUROSCI.1350-11.2011>
- Dzhala V**, Valeeva G, Glykys J, Khazipov R, Staley K. 2012. Traumatic alterations in GABA signaling disrupt hippocampal network activity in the developing brain. *Journal of Neuroscience* **32**:4017–4031. DOI: <https://doi.org/10.1523/JNEUROSCI.5139-11.2012>, PMID: 22442068
- Eccles JC**, Llinás R, Sasaki K. 1966. The inhibitory interneurons within the cerebellar cortex. *Experimental Brain Research* **1**:1–16. DOI: <https://doi.org/10.1007/BF00235206>
- Evangelidis GD**, Psarakis EZ. 2008. Parametric image alignment using enhanced correlation coefficient maximization. *IEEE Transactions on Pattern Analysis and Machine Intelligence* **30**:1858–1865. DOI: <https://doi.org/10.1109/TPAMI.2008.113>, PMID: 18703836
- Eybalin M**, Caicedo A, Renard N, Ruel J, Puel JL. 2004. Transient Ca<sup>2+</sup>-permeable AMPA receptors in postnatal rat primary auditory neurons. *European Journal of Neuroscience* **20**:2981–2989. DOI: <https://doi.org/10.1111/j.1460-9568.2004.03772.x>, PMID: 15579152
- Finch EA**, Augustine GJ. 1998. Local calcium signalling by inositol-1,4,5-trisphosphate in purkinje cell dendrites. *Nature* **396**:753–756. DOI: <https://doi.org/10.1038/25541>, PMID: 9874372
- Franconville R**, Revet G, Astorga G, Schwaller B, Llano I. 2011. Somatic calcium level reports integrated spiking activity of cerebellar interneurons in vitro and in vivo. *Journal of Neurophysiology* **106**:1793–1805. DOI: <https://doi.org/10.1152/jn.00133.2011>, PMID: 21734102
- Gaffield MA**, Christie JM. 2017. Movement rate is encoded and influenced by widespread, coherent activity of cerebellar molecular layer interneurons. *The Journal of Neuroscience* **37**:4751–4765. DOI: <https://doi.org/10.1523/JNEUROSCI.0534-17.2017>, PMID: 28389475
- Glitsch M**, Marty A. 1999. Presynaptic effects of NMDA in cerebellar purkinje cells and interneurons. *The Journal of Neuroscience* **19**:511–519. DOI: <https://doi.org/10.1523/JNEUROSCI.19-02-00511.1999>, PMID: 9880571
- Grandes P**, Mateos JM, Rüegg D, Kuhn R, Knöpfel T. 1994. Differential cellular localization of three splice variants of the mGluR1 metabotropic glutamate receptor in rat cerebellum. *NeuroReport* **5**:2249–2252. DOI: <https://doi.org/10.1097/00001756-199411000-00011>, PMID: 7881038
- Graupner M**. 2020. mGluR\_MLI\_in-vivo. *GitHub*. e138f46. [https://github.com/mgraupe/mGluR\\_MLI\\_in-vivo](https://github.com/mgraupe/mGluR_MLI_in-vivo)
- Hartmann J**, Konnerth A. 2009. Mechanisms of metabotropic glutamate receptor-mediated synaptic signalling in cerebellar purkinje cells. *Acta Physiologica* **195**:79–90. DOI: <https://doi.org/10.1111/j.1748-1716.2008.01923.x>
- Hippenmeyer S**, Vrieseling E, Sigrist M, Portmann T, Laengle C, Ladle DR, Arber S. 2005. A developmental switch in the response of DRG neurons to ETS transcription factor signaling. *PLOS Biology* **3**:e159. DOI: <https://doi.org/10.1371/journal.pbio.0030159>, PMID: 15836427
- Isaac JT**, Ashby MC, McBain CJ. 2007. The role of the GluR2 subunit in AMPA receptor function and synaptic plasticity. *Neuron* **54**:859–871. DOI: <https://doi.org/10.1016/j.neuron.2007.06.001>, PMID: 17582328
- Jelitai M**, Puggioni P, Ishikawa T, Rinaldi A, Duguid I. 2016. Dendritic excitation-inhibition balance shapes cerebellar output during motor behaviour. *Nature Communications* **7**:13722. DOI: <https://doi.org/10.1038/ncomms13722>, PMID: 27976716
- Jörntell H**. 2017. Cerebellar physiology: links between microcircuitry properties and sensorimotor functions. *The Journal of Physiology* **595**:11–27. DOI: <https://doi.org/10.1113/JP272769>, PMID: 27388692

- Jörntell H, Ekerot CF. 2006. Properties of somatosensory synaptic integration in cerebellar granule cells in vivo. *Journal of Neuroscience* **26**:11786–11797. DOI: <https://doi.org/10.1523/JNEUROSCI.2939-06.2006>, PMID: 17093099
- Kano M, Hashimoto K, Tabata T. 2008. Type-1 metabotropic glutamate receptor in cerebellar purkinje cells: a key molecule responsible for long-term depression, endocannabinoid signalling and synapse elimination. *Philosophical Transactions of the Royal Society B: Biological Sciences* **363**:2173–2186. DOI: <https://doi.org/10.1098/rstb.2008.2270>
- Karakossian MH, Otis TS. 2004. Excitation of cerebellar interneurons by group I metabotropic glutamate receptors. *Journal of Neurophysiology* **92**:1558–1565. DOI: <https://doi.org/10.1152/jn.00300.2004>, PMID: 15152021
- Kelly L, Farrant M, Cull-Candy SG. 2009. Synaptic mGluR activation drives plasticity of calcium-permeable AMPA receptors. *Nature Neuroscience* **12**:593–601. DOI: <https://doi.org/10.1038/nn.2309>
- Kim JK, Choi JW, Lim S, Kwon O, Seo JK, Ryu SH, Suh PG. 2011. Phospholipase C- $\eta$ 1 is activated by intracellular Ca(2+) mobilization and enhances GPCRs/PLC/Ca(2+) signaling. *Cellular Signalling* **23**:1022–1029. DOI: <https://doi.org/10.1016/j.cellsig.2011.01.017>, PMID: 21262355
- Knöpfel T, Grandes P. 2002. Metabotropic glutamate receptors in the cerebellum with a focus on their function in purkinje cells. *The Cerebellum* **1**:19–26. DOI: <https://doi.org/10.1007/BF02941886>, PMID: 12879970
- Kuhn B, Ozden I, Lampi Y, Hasan MT, Wang SS. 2012. An amplified promoter system for targeted expression of calcium indicator proteins in the cerebellar cortex. *Frontiers in Neural Circuits* **6**:49. DOI: <https://doi.org/10.3389/fncir.2012.00049>, PMID: 22866030
- Kumar SS, Bacci A, Kharazia V, Huguenard JR. 2002. A developmental switch of AMPA receptor subunits in neocortical pyramidal neurons. *The Journal of Neuroscience* **22**:3005–3015. DOI: <https://doi.org/10.1523/JNEUROSCI.22-08-03005.2002>, PMID: 11943803
- Liu Y, Formisano L, Savtchouk I, Takayasu Y, Szabó G, Zukin RS, Liu SJ. 2010. A single fear-inducing stimulus induces a transcription-dependent switch in synaptic AMPAR phenotype. *Nature Neuroscience* **13**:223–231. DOI: <https://doi.org/10.1038/nn.2474>, PMID: 20037575
- Liu SQ, Cull-Candy SG. 2000. Synaptic activity at calcium-permeable AMPA receptors induces a switch in receptor subtype. *Nature* **405**:454–458. DOI: <https://doi.org/10.1038/35013064>, PMID: 10839540
- Lujan R, Nusser Z, Roberts JD, Shigemoto R, Somogyi P. 1996. Perisynaptic location of metabotropic glutamate receptors mGluR1 and mGluR5 on dendrites and dendritic spines in the rat Hippocampus. *European Journal of Neuroscience* **8**:1488–1500. DOI: <https://doi.org/10.1111/j.1460-9568.1996.tb01611.x>, PMID: 8758956
- Luján R, Roberts JD, Shigemoto R, Ohishi H, Somogyi P. 1997. Differential plasma membrane distribution of metabotropic glutamate receptors mGluR1 Alpha, mGluR2 and mGluR5, relative to neurotransmitter release sites. *Journal of Chemical Neuroanatomy* **13**:219–241. DOI: [https://doi.org/10.1016/S0891-0618\(97\)00051-3](https://doi.org/10.1016/S0891-0618(97)00051-3), PMID: 9412905
- Magazanik LG, Buldakova SL, Samoilova MV, Gmiro VE, Mellor IR, Usherwood PN. 1997. Block of open channels of recombinant AMPA receptors and native AMPA/kainate receptors by adamantane derivatives. *The Journal of Physiology* **505**:655–663. DOI: <https://doi.org/10.1111/j.1469-7793.1997.655ba.x>, PMID: 9457643
- Mansouri M, Kasugai Y, Fukazawa Y, Bertaso F, Raynaud F, Perroy J, Fagni L, Kaufmann WA, Watanabe M, Shigemoto R, Ferraguti F. 2015. Distinct subsynaptic localization of type 1 metabotropic glutamate receptors at Glutamatergic and GABAergic synapses in the rodent cerebellar cortex. *European Journal of Neuroscience* **41**:157–167. DOI: <https://doi.org/10.1111/ejn.12779>, PMID: 25377770
- Masugi-Tokita M, Tarusawa E, Watanabe M, Molnár E, Fujimoto K, Shigemoto R. 2007. Number and density of AMPA receptors in individual synapses in the rat cerebellum as revealed by SDS-digested freeze-fracture replica labeling. *Journal of Neuroscience* **27**:2135–2144. DOI: <https://doi.org/10.1523/JNEUROSCI.2861-06.2007>, PMID: 17314308
- Nicholson E, Kullmann DM. 2017. T-type calcium channels contribute to NMDA receptor independent synaptic plasticity in hippocampal regular-spiking oriens-alveus interneurons. *The Journal of Physiology* **595**:3449–3458. DOI: <https://doi.org/10.1113/JP273695>, PMID: 28134447
- Okubo Y, Kakizawa S, Hirose K, Iino M. 2004. Cross talk between metabotropic and ionotropic glutamate receptor-mediated signaling in parallel fiber-induced inositol 1,4,5-trisphosphate production in cerebellar purkinje cells. *Journal of Neuroscience* **24**:9513–9520. DOI: <https://doi.org/10.1523/JNEUROSCI.1829-04.2004>, PMID: 15509738
- Ozden I, Dombek DA, Hoogland TM, Tank DW, Wang SS. 2012. Widespread state-dependent shifts in cerebellar activity in locomoting mice. *PLOS ONE* **7**:e42650. DOI: <https://doi.org/10.1371/journal.pone.0042650>, PMID: 22880068
- Pachitariu M, Stringer C, Dipoppa M, Schröder S RLF, Dalgleish H, Carandini M, Harris KD. 2007. Suite2p: beyond 10,000 neurons with standard two-photon microscopy. *bioRxiv*. DOI: <https://doi.org/10.1101/061507>
- Palay SL, Chan-Palay V. 1974. *Cerebellar Cortex: Cytology and Organization*. Berlin: Springer.
- Pologruto TA, Sabatini BL, Svoboda K. 2003. ScanImage: flexible software for operating laser scanning microscopes. *Biomedical Engineering Online* **2**:13. DOI: <https://doi.org/10.1186/1475-925X-2-13>, PMID: 12801419
- Provini L, Redman S, Strata P. 1968. Mossy and climbing fibre organization on the anterior lobe of the cerebellum activated by forelimb and hindlimb Areas of the sensorimotor cortex. *Experimental Brain Research* **6**:216–233. DOI: <https://doi.org/10.1007/BF00235125>, PMID: 5712701

- Reiner A**, Levitz J. 2018. Glutamatergic signaling in the central nervous system: ionotropic and metabotropic receptors in concert. *Neuron* **98**:1080–1098. DOI: <https://doi.org/10.1016/j.neuron.2018.05.018>, PMID: 29953871
- Rossi B**, Maton G, Collin T. 2008. Calcium-permeable presynaptic AMPA receptors in cerebellar molecular layer interneurons. *The Journal of Physiology* **586**:5129–5145. DOI: <https://doi.org/10.1113/jphysiol.2008.159921>, PMID: 18772200
- Rowan MJM**, Bonnan A, Zhang K, Amat SB, Kikuchi C, Taniguchi H, Augustine GJ, Christie JM. 2018. Graded control of Climbing-Fiber-Mediated plasticity and learning by inhibition in the cerebellum. *Neuron* **99**:999–1015. DOI: <https://doi.org/10.1016/j.neuron.2018.07.024>, PMID: 30122378
- Shigemoto R**, Kinoshita A, Wada E, Nomura S, Ohishi H, Takada M, Flor PJ, Neki A, Abe T, Nakanishi S, Mizuno N. 1997. Differential presynaptic localization of metabotropic glutamate receptor subtypes in the rat Hippocampus. *The Journal of Neuroscience* **17**:7503–7522. DOI: <https://doi.org/10.1523/JNEUROSCI.17-19-07503.1997>, PMID: 9295396
- Soler-Llavina GJ**, Sabatini BL. 2006. Synapse-specific plasticity and compartmentalized signaling in cerebellar stellate cells. *Nature Neuroscience* **9**:798–806. DOI: <https://doi.org/10.1038/nn1698>, PMID: 16680164
- Sullivan MR**, Nimmerjahn A, Sarkisov DV, Helmchen F, Wang SS-H. 2005. In vivo calcium imaging of circuit activity in cerebellar cortex. *Journal of Neurophysiology* **94**:1636–1644. DOI: <https://doi.org/10.1152/jn.01013.2004>
- Sylantsev S**, Savtchenko LP, Ermolyuk Y, Michaluk P, Rusakov DA. 2013. Spike-driven glutamate electrodiffusion triggers synaptic potentiation via a homer-dependent mGluR-NMDAR link. *Neuron* **77**:528–541. DOI: <https://doi.org/10.1016/j.neuron.2012.11.026>, PMID: 23395378
- Takechi H**, Eilers J, Konnerth A. 1998. A new class of synaptic response involving calcium release in dendritic spines. *Nature* **396**:757–760. DOI: <https://doi.org/10.1038/25547>, PMID: 9874373
- Tian L**, Hires SA, Mao T, Huber D, Chiappe ME, Chalasani SH, Petreanu L, Akerboom J, McKinney SA, Schreiner ER, Bargmann CI, Jayaraman V, Svoboda K, Looger LL. 2009. Imaging neural activity in worms, flies and mice with improved GCaMP calcium indicators. *Nature Methods* **6**:875–881. DOI: <https://doi.org/10.1038/nmeth.1398>, PMID: 19898485
- Uesaka N**, Uchigashima M, Mikuni T, Nakazawa T, Nakao H, Hirai H, Aiba A, Watanabe M, Kano M. 2014. Retrograde semaphorin signaling regulates synapse elimination in the developing mouse brain. *Science* **344**:1020–1023. DOI: <https://doi.org/10.1126/science.1252514>, PMID: 24831527
- Wang X**, Chen G, Gao W, Ebner TJ. 2011. Parasagittally aligned, mGluR1-dependent patches are evoked at long latencies by parallel fiber stimulation in the mouse cerebellar cortex in vivo. *Journal of Neurophysiology* **105**:1732–1746. DOI: <https://doi.org/10.1152/jn.00717.2010>, PMID: 21289138
- Welsh JP**, Yamaguchi H, Zeng XH, Kojo M, Nakada Y, Takagi A, Sugimori M, Llinás RR. 2005. Normal motor learning during pharmacological prevention of purkinje cell long-term depression. *PNAS* **102**:17166–17171. DOI: <https://doi.org/10.1073/pnas.0508191102>, PMID: 16278298
- Wulff P**, Schonewille M, Renzi M, Viltono L, Sassoè-Pognetto M, Badura A, Gao Z, Hoebeek FE, van Dorp S, Wisden W, Farrant M, De Zeeuw CI. 2009. Synaptic inhibition of purkinje cells mediates consolidation of vestibulo-cerebellar motor learning. *Nature Neuroscience* **12**:1042–1049. DOI: <https://doi.org/10.1038/nn.2348>, PMID: 19578381
- Zariwala HA**, Borghuis BG, Hoogland TM, Madisen L, Tian L, De Zeeuw CI, Zeng H, Looger LL, Svoboda K, Chen TW. 2012. A Cre-dependent GCaMP3 reporter mouse for neuronal imaging in vivo. *Journal of Neuroscience* **32**:3131–3141. DOI: <https://doi.org/10.1523/JNEUROSCI.4469-11.2012>, PMID: 22378886
- Zhao S**, Ting JT, Atallah HE, Qiu L, Tan J, Gloss B, Augustine GJ, Deisseroth K, Luo M, Graybiel AM, Feng G. 2011. Cell type-specific channelrhodopsin-2 transgenic mice for optogenetic dissection of neural circuitry function. *Nature Methods* **8**:745–752. DOI: <https://doi.org/10.1038/nmeth.1668>, PMID: 21985008
- Zheng N**, Raman IM. 2011. Prolonged postinhibitory rebound firing in the cerebellar nuclei mediated by group I metabotropic glutamate receptor potentiation of L-type calcium currents. *Journal of Neuroscience* **31**:10283–10292. DOI: <https://doi.org/10.1523/JNEUROSCI.1834-11.2011>, PMID: 21753005